Molecular Therapy
Original Article

DLK1/DIO3 locus upregulation by a β-catenin-dependent enhancer drives cell proliferation and liver tumorigenesis

Julie Sanceau,[1,2,3] Lucie Poupel,[1,2,3,4] Camille Joubel,[1,2,3] Isabelle Lagoutte,[5] Stefano Caruso,[1,3] Sandra Pinto,[1,2] Christèle Desbois-Mouthon,[1,2,3] Cécile Godard,[1,2,3] Akila Hamimi,[1,2,3] Enzo Montmory,[1,2,3] Cécile Dulary,[6] Sophie Chantalat,[6] Amélie Roehrig,[1,3] Kevin Muret,[6] Benjamin Saint-Pierre,[5] Jean-François Deleuze,[6] Sophie Mouillet-Richard,[1,3] Thierry Forné,[7] Christophe F. Grosset,[8,9] Jessica Zucman-Rossi,[1,3] Sabine Colnot,[1,2,3] and Angélique Gougelet[1,2,3]

[1]Centre de Recherche des Cordeliers, Sorbonne Université, Inserm, Université Paris Cité, F-75006 Paris, France; [2]Team « Oncogenic functions of beta-catenin signaling in the liver », Équipe labellisée par la Ligue Nationale contre le Cancer, F-75013 Paris, France; [3]APHP, Institut du Cancer Paris CARPEM, F-75015 Paris, France; [4]Inovarion, F-75005 Paris, France; [5]University Paris Cité, Institut Cochin, INSERM, CNRS, F-75014 Paris, France; [6]Centre National de Génotypage, Institut de Génomique, CEA, F-91057 Evry, France; [7]IGMM, University Montpellier, CNRS, F-34293 Montpellier, France; [8]University Bordeaux, INSERM, Biotherapy of Genetic Diseases, Inflammatory Disorders and Cancer, BMGIC, U1035, MIRCADE team, F-33076 Bordeaux, France; [9]University Bordeaux, INSERM, Bordeaux Institute in Oncology, BRIC, U1312, MIRCADE team, F-33076 Bordeaux, France

The *CTNNB1* gene, encoding β-catenin, is frequently mutated in hepatocellular carcinoma (HCC, ∼30%) and in hepatoblastoma (HB, >80%), in which *DLK1/DIO3* locus induction is correlated with *CTNNB1* mutations. Here, we aim to decipher how sustained β-catenin activation regulates *DLK1/DIO3* locus expression and the role this locus plays in HB and HCC development in mouse models deleted for *Apc* ($Apc^{\Delta hep}$) or *Ctnnb1-exon 3* ($\beta\text{-catenin}^{\Delta Exon3}$) and in human *CTNNB1*-mutated hepatic cancer cells. We identified an enhancer site bound by TCF-4/β-catenin complexes in an open conformation upon sustained β-catenin activation (DLK1-Wnt responsive element [WRE]) and increasing *DLK1/DIO3* locus transcription in β-catenin-mutated human HB and mouse models. DLK1-WRE editing by CRISPR-Cas9 approach impaired *DLK1/DIO3* locus expression and slowed tumor growth in subcutaneous *CTNNB1*-mutated tumor cell grafts, $Apc^{\Delta hep}$ HB and $\beta\text{-catenin}^{\Delta Exon3}$ HCC. Tumor growth inhibition resulted either from increased FADD expression and subsequent caspase-3 cleavage in the first case or from decreased expression of cell cycle actors regulated by FoxM1 in the others. Therefore, the *DLK1/DIO3* locus is an essential determinant of FoxM1-dependent cell proliferation during β-catenin-driven liver tumorigenesis. Targeting the DLK1-WRE enhancer to silence the *DLK1/DIO3* locus might thus represent an interesting therapeutic strategy to restrict tumor growth in primary liver cancers with *CTNNB1* mutations.

INTRODUCTION

The two most common primary liver tumors, hepatocellular carcinoma (HCC) in adults and hepatoblastoma (HB) in children, are both characterized by mutations in the Wnt/β-catenin pathway. Somatic point mutations in the *CTNNB1* gene, encoding β-catenin, are encountered in approximately 30% of HCC[1] and *CTNNB1* exon 3 deletions occur in more than 80% of HB.[2,3] *CTNNB1* mutations prevent β-catenin phosphorylation and its subsequent proteasomal degradation orchestrated by a complex containing APC, AXIN1, GSK3β, and CK1. This leads to β-catenin stabilization and translocation into the nucleus, where, in hepatocytes, it interacts primarily with TCF-4 before recruitment at Wnt responsive elements (WREs).[4] This recruitment allows the regulation of a specific gene repertoire acting on metabolic and proliferative pathways.[5,6] To finely tune its gene repertoire, β-catenin is able to cooperate with a plethora of histone modifiers and chromatin remodelers,[7] numbers of them being mutated in HCC.[8]

In HB, additional mutations can also affect chromatin modifiers or long non-coding RNAs (lncRNAs) produced from parentally imprinted clusters, such as *H19* or *MEG3*.[9,10] The *DLK1/DIO3* locus encodes the largest cluster of non-coding RNAs (ncRNAs), including 54 microRNAs (miRNAs), several small nucleolar RNAs (snoRNAs), and lncRNAs (e.g., *MEG3*, *MEG8*/*RIAN*, *MEG9*/*MIRG*) expressed from the maternal allele but also encoding paternally expressed RNAs such as *DLK1*, *RTL1*, and *DIO3* (Figure 1A). The expression of the *DLK1/DIO3* locus is mainly regulated by methylation of three differentially methylated regions (DMRs), named DLK1-, IG-, and MEG3-DMRs, with different regulatory functions.[11] This imprinted

Received 1 December 2023; accepted 31 January 2024;
https://doi.org/10.1016/j.ymthe.2024.01.036.

Correspondence: Angélique Gougelet, Centre de Recherche des Cordeliers, 15, rue de l'école de médecine, 75006 Paris, France.
E-mail: angelique.gougelet@inserm.fr

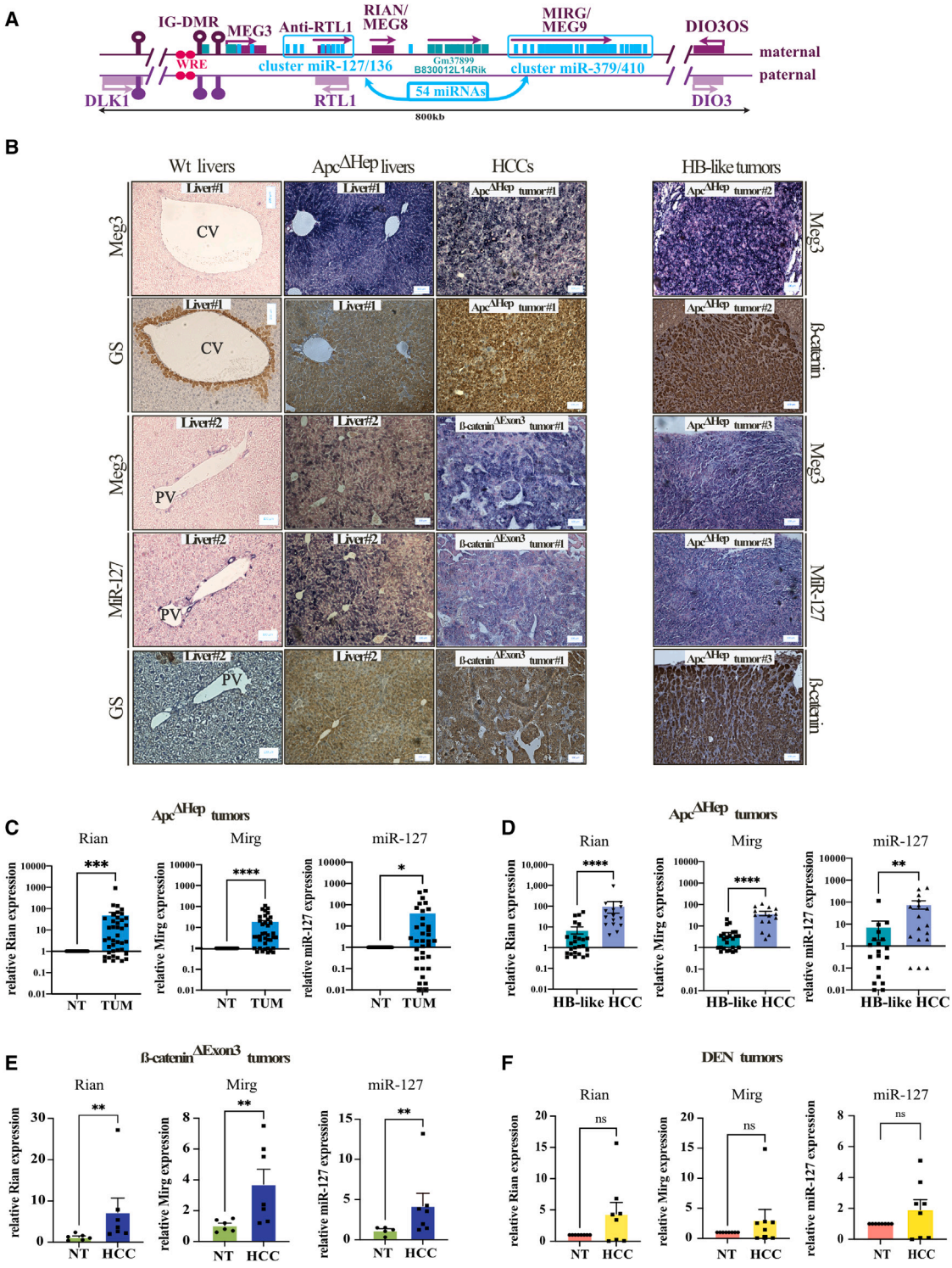

Figure 1. The *Dlk1/Dio3* locus is induced in mouse HCC- and HB-like tumors driven by β-catenin

(A) Schematic representation of the *DLK1/DIO3* locus. (B) *In situ* hybridization of *Meg3* and miR-127 with staining of glutamine synthetase (GS) or active β-catenin in WT and Apc$^{\Delta hep}$ livers and in Apc$^{\Delta hep}$ and β-catenin$^{\Delta Exon3}$ HCC- or HB-like tumors. CV, central vein; PV, portal vein. (C–F) Expression of *Rian*, *Mirg*, and miR-127 with error bars representing SEM by RT-qPCR in Apc$^{\Delta hep}$ tumors (TUM) compared to adjacent non-tumor (NT) tissue (C); in Apc$^{\Delta hep}$ HCC and HB-like tumors (D); in β-catenin$^{\Delta Exon3}$ tumors (E); and in DEN tumors without β-catenin activation (F). *p < 0.05, **p < 0.01, ***p < 0.005, ****p < 0.0001; ns, non-significant (Mann-Whitney).

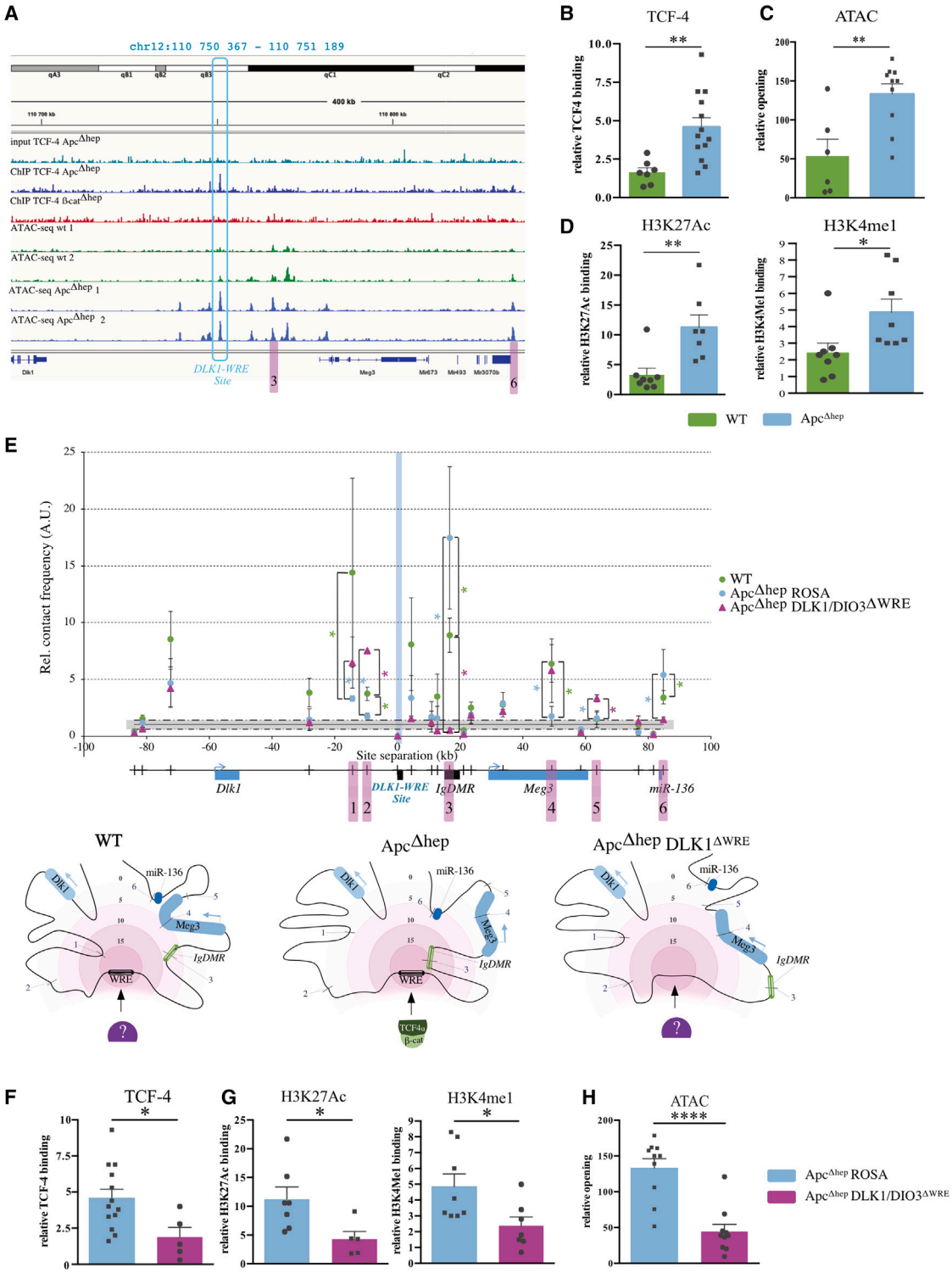

Figure 2. β-Catenin binding at the DLK1-WRE site opens chromatin and exerts enhancer activity in Apc$^{\Delta hep}$ hepatocytes

(A) ChIP-seq targeting TCF-4 in WT, Apc$^{\Delta hep}$, and β-cat$^{\Delta hep}$ hepatocytes and ATAC-seq data in WT and Apc$^{\Delta hep}$ hepatocytes. TCF-4 binding site is framed in the blue box (DLK1-WRE) and sites common with 3C in pink. (B, D, F, and G) ChIP-qPCR analysis at the DLK1-WRE site for TCF-4, H3K4me1, and H3K27ac relative to isotype control in Apc$^{\Delta hep}$ hepatocytes with error bars representing SEM compared to WT (B and D) and compared to Apc$^{\Delta hep}$-DLK1/DIO3$^{\Delta WRE}$ hepatocytes (F and G). (C and H) ATAC-qPCR

(legend continued on next page)

locus is crucial for cell pluripotency[12] and liver metabolic adaptation.[13] RNAs produced from the *DLK1/DIO3* locus are frequently underexpressed in cancers,[14] either under- or overexpressed in HCC,[15,16] while *DLK1/DIO3* locus induction in HB is associated with poor prognosis[17,18] and *CTNNB1* mutations.[18]

In the present study, we decipher the molecular mechanisms whereby sustained β-catenin activation affects gene expression at the *DLK1/DIO3* locus and the role that this activation plays in the development of primary liver cancers. We used two mouse models that develop HCC or HB following oncogenic activation of β-catenin signaling through either inducible and liver-specific loss of function of *Apc* ($Apc^{\Delta hep}$)[5,19–22] or deletion of *Ctnnb1-exon 3* (β-$catenin^{\Delta Exon3}$).[23] Using *in vivo* CRISPR-Cas9 editing, we identified a new regulatory site upstream of *Meg3* (DLK1-WRE site) bound by oncogenic β-catenin/TCF-4 complexes and responsible for *Dlk1/Dio3* locus induction. We also demonstrated the crucial pro-tumorigenic role of the *DLK1/DIO3* locus in the regulation of apoptosis and FoxM1-driven cell cycle progression during liver carcinogenesis mediated by β-catenin in both mouse models and in hepatic cancer cell lines.

RESULTS

The *Dlk1/Dio3* locus is induced after sustained β-catenin activation in mouse livers and tumors

Our team has created two mouse models that recapitulate liver cancer development with sustained β-catenin activation, either Cre-Lox-based *Apc* excision ($Apc^{\Delta hep}$) or CRISPR-Cas9 deletion of *Ctnnb1-exon 3* (β-$catenin^{\Delta Exon3}$) (Figures S1A–S1C).[23] In both models, two tumor types can emerge from healthy livers: either well-differentiated HCC similar to human G5-G6 HCC or poorly differentiated tumors close to human HB. Human tumors and mouse tumors from both models share dysregulated transcriptional programs.[23]

RNA sequencing (RNA-seq) and small RNA-seq data showed that coding RNAs and ncRNAs within the *Dlk1/Dio3* locus were some of the most significantly overexpressed RNAs in preneoplastic $Apc^{\Delta hep}$ hepatocytes compared to wild-type (WT) (Tables S1 and S2).[5,21] Induction of *Meg3* and miR-127 was confirmed by *in situ* hybridization in $Apc^{\Delta hep}$ hepatocytes as well as in $Apc^{\Delta hep}$ and β-$catenin^{\Delta Exon3}$ HCC and HB-like tumors (Figure 1B). Upregulation of *Mirg*, *Rian*, and miR-127 was confirmed by RT-qPCR in $Apc^{\Delta hep}$ tumors (TUM) relative to adjacent non-tumor tissues (NT) (Figure 1C). It was found stronger in HCC compared to HB (Figure 1D) in agreement with the maintenance of metabolic targets in HCC harboring hepatocyte features.[23,24] The locus induction also appeared higher in $Apc^{\Delta hep}$ HCC compared to β-$catenin^{\Delta Exon3}$ HCC (compare Figure 1D/1E). It is also noteworthy that strong correlations between RNA expression levels of *Rian*, *Mirg*, miR-127, and *Glul*, a canonical β-catenin target, were found both in $Apc^{\Delta hep}$ (Figure S2A) and β-$catenin^{\Delta Exon3}$ tumors (Figure S2B). In diethylnitrosamine (DEN)-induced livers tumors without *Glul* induction, the expression of *Rian*, *Mirg*, and miR-127 was not modified (Figure 1F) and no correlation with *Glul* was observed (Figure S2C).

Using a Cre-GFP adenovirus, we sorted GFP+ $Apc^{\Delta hep}$ hepatocytes during the earliest steps of liver tumorigenesis (Figure S1D). RNA-seq data showed that all RNAs within the *Dlk1/Dio3* locus were induced between 6 and 15 days after *Apc* inactivation compared to non-activated GFP− hepatocytes (Figure S3A), similarly to canonical β-catenin targets such as *Glul* or *Axin2* (Figure S3B).

These results indicate that sustained β-catenin activation correlates with coordinated upregulation of ncRNAs within the *Dlk1/Dio3* locus in preneoplastic hepatocytes and mouse tumors.

TCF-4/β-catenin complexes bind upstream of *Meg3* promoting an enhancer activation

Our next objective was to decipher how β-catenin activation promotes *Dlk1/Dio3* locus expression. Our chromatin immunoprecipitation (ChIP) sequencing (ChIP-seq) data targeting the β-catenin cofactor TCF-4 in $Apc^{\Delta hep}$ hepatocytes showed that TCF-4 bound upstream of *Meg3* to a site containing two canonical WRE motifs (named DLK1-WRE) (Figures 2A and S5A). TCF-4 binding was conserved in the human HepG2 cell line with activating *CTNNB1* mutations (public dataset GSM782122) (Figures 3A and S5H). TCF-4 did not bind to the DLK1-WRE site in hepatocytes isolated from a mouse model invalidated for β-catenin (β-$cat^{\Delta hep}$ in Figure 2A). Impaired expression of non-coding RNAs within the *Dlk1/Dio3* locus was subsequently noticed in β-$cat^{\Delta hep}$ hepatocytes (Tables S1 and S2). ChIP-qPCR targeting the DLK1-WRE site confirmed increased binding of both TCF-4 (Figure 2B) and β-catenin (Figure S4A) in $Apc^{\Delta hep}$ hepatocytes compared to WT hepatocytes. Assay for transposase-accessible chromatin (ATAC) with sequencing (ATAC-seq) (Figure 2A) and ATAC-qPCR experiments (Figure 2C) indicated an open chromatin configuration at the DLK1-WRE site in $Apc^{\Delta hep}$ hepatocytes. Identical results were obtained from β-$catenin^{\Delta exon3}$ hepatocytes for TCF-4 binding and open chromatin conformation (Figure S4B).

H3K4me1 and H3K27ac ChIP-qPCR experiments showed that these typical marks of enhancers were both found significantly increased at the DLK1-WRE site in $Apc^{\Delta hep}$ and β-$catenin^{\Delta exon3}$ hepatocytes compared to WT hepatocytes (Figures 2D and S4B). No significant differences were found for the H3K4me3 mark associated with transcriptionally active chromatin at transcription start sites (Figure S4C). Increased TCF-4 binding was also detected at the DLK1-WRE site in

analysis at the DLK1-WRE site compared to WT (C) and to $Apc^{\Delta hep}$-DLK1/$DIO3^{\Delta WRE}$ hepatocytes (H). (E) Relative contact frequencies in arbitrary units (a.u.) between the DLK1-WRE site (blue vertical bar) and 19 genomic sites (small vertical black bars on the map below) measured in 3C experiments performed on WT, $Apc^{\Delta hep}$-Rosa26, and $Apc^{\Delta hep}$-DLK1/$DIO3^{\Delta WRE}$ liver nuclei with error bars representing SEM of six, five, and three biological replicates, respectively. Regions of interest (highlighted in pink) are numbered from 1 to 6. The lower panel illustrates the different chromatin loops distributed into six interaction zones: the darker the pink, the stronger the interaction. Figure made with BioRender. *$p < 0.05$, **$p < 0.01$, ***$p < 0.005$, ****$p < 0.0001$; ns, non-significant (Mann-Whitney).

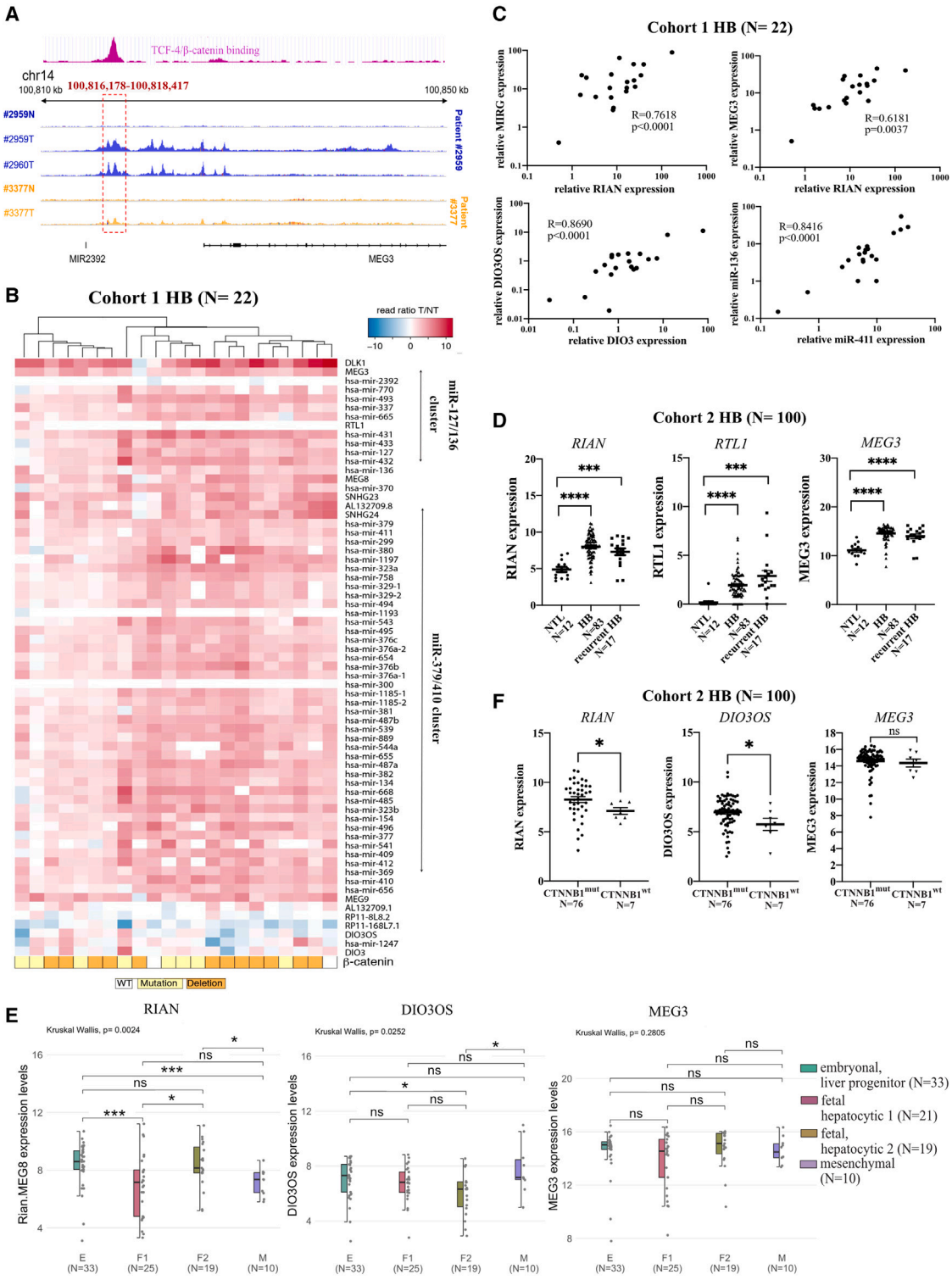

Figure 3. The *DLK1/DIO3* locus is induced in human HB in correlation with *CTNNB1* mutations and DLK1-WRE opening

(A) Pseudo bulk snATAC-seq aggregated with Cellranger-atac of three human HBs (T) and their adjacent NT tissue (N) at the DLK1-WRE site; the pink panel represents ChIP-seq data targeting TCF-4 in the human HB HepG2 cell line (Gsm782122). (B) RNA-seq expression data for the entire DLK1/DIO3 locus in HB normalized to their adjacent NT tissue (N = 22, cohort 1). A white square in the β-catenin lane indicates HB with intact *CTNNB1*, a yellow square HB with point mutation in *CTNNB1*, an orange square HB with

(legend continued on next page)

Apc$^{\Delta hep}$ and β-catenin$^{\Delta exon3}$ tumors compared to non-tumor tissues (Figure S4D). Remarkably, no modification in DNA methylation profiles and TCF-4 binding was observed at the IG-DMR in Apc$^{\Delta hep}$ hepatocytes compared to WT hepatocytes (Figures S4E–S4F).[22]

Interestingly, HNF4α, a transcriptional factor involved in hepatocyte differentiation, bound to the DLK1-WRE site in Apc$^{\Delta hep}$ hepatocytes and independently of TCF-4 binding since its binding was not affected in Apc$^{\Delta hep}$ DLK1$^{\Delta WRE}$ hepatocytes (Figure S4G). In addition, HNF4α was not co-immunoprecipitated with TCF-4 at the DLK1-WRE site in sequential ChIP experiments (Figure S4H). HNF4α binding favored *Meg3* and *miR-127* expression since their expression was impaired in HNF4α$^{\Delta hep}$ hepatocytes (Figure S4I), consistent with previous data.[25] HNF4α binding could therefore contribute in the higher expression of the locus observed in HCC (Figure 1D), in which HNF4α expression is maintained in contrast to HB (PRJEB44400 dataset).[23]

Globally, these results demonstrate that, upon sustained β-catenin activation, a DLK1-WRE site located upstream of *Meg3*, bound by TCF-4/β-catenin complexes, is in an open configuration and marked by histone modifications typical of active enhancers. We can assume that TCF-4/β-catenin binding at this site promotes the formation of an active enhancer favoring transcription of the entire *Dlk1/Dio3* locus.

Besides its transcriptional role, β-catenin is able to bridge distal DNA regions by chromatin looping.[7] The tridimensional organization of the *DLK1/DIO3* locus is also known to be highly dynamic according to its expression patterns during embryonic development.[26,27] We thus investigated whether, following oncogenic TCF-4/β-catenin binding, the activation of the putative DLK1-WRE enhancer could affect the tridimensional organization of the *DLK1/DIO3* locus. To this aim, we performed a 3C-qPCR analysis centered on the DLK1-WRE site and covering the region between DLK1 and miR-136. The relative contact frequencies measured all along the locus allow specific interactions to be determined: the higher the frequency, the closer the DNA region is relative to the DLK1-WRE site (vertical blue bar in Figure 2E). In WT hepatocytes (Figure 2E, green dots), six major regions are interacting with the DLK1-WRE site: one located upstream of *Dlk1*, two regions in the vicinity of the DLK1-WRE site (sites 1 and 2), one site within the Ig-DMR (site 3), one within *Meg3* (site 4), and one in the miR-136 region (site 6). In Apc$^{\Delta hep}$ hepatocytes (Figure 2E, blue dots), binding of TCF-4 to the DLK1-WRE site resulted in drastic DNA loop remodeling. Interactions with sites 1, 2, and 4 were lost, while looping with the Ig-DMR (site 3) and the miR-136 region (site 6) were reinforced. Remarkably, these two loops coincided with two open chromatin regions observed by ATAC-seq in Apc$^{\Delta hep}$ hepatocytes (sites 3 and 6 highlighted in pink in Figure 2A).

We conclude that, in Apc$^{\Delta hep}$ hepatocytes, oncogenic β-catenin/TCF-4 complexes bound at the DLK1-WRE site largely modify 3D chromatin organization and favor interactions with coding regions located after the Ig-DMR rather than upstream regions. This important re-organization may thus contribute to upregulate the expression of the non-coding RNAs encoded in the downstream part of the *DLK1/DIO3* locus.

The DLK1-WRE regulatory site is conserved in human HB

Consistent with our observations in mouse models and as mentioned above, we identified a TCF-4 binding site upstream of *MEG3* in HepG2 cells, a human HB cell line harboring a *CTNNB1* deletion (Figures 3A and S5H) (GSM782122). Multiome single-nucleus ATAC-seq (snATAC-seq) experiments conducted on samples from two HB patients harboring *CTNNB1* mutations showed that the human DLK1-WRE site was in an open conformation in HB compared to their paired adjacent non-tumor tissues (Figure 3A). The expression of miRNAs, as well as lncRNAs and coding RNAs, from the *DLK1/DIO3* locus was increased in both 20 *CTNNB1*-mutated HB (yellow and orange squares in Figure 3B) and two non-mutated HBs (white square in Figure 3B) compared to their paired adjacent non-tumor tissues (Table S3). Interestingly, a strong correlation was observed between expressions of the different ncRNAs (Figure 3C), supporting the idea of a global induction of this region in human HB. Overexpression of these ncRNAs was confirmed in an independent larger collection of primary (n = 83) and recurrent HB (n = 17) (Figure 3D; Table S4), and regardless of the HB subgroups (Figure 3E). In this collection containing a higher number of non-mutated HBs (n = 7), we found that *RIAN* and *DIO3OS* expression was even significantly higher in *CTNNB1*-mutated HB compared to non-mutated HB, with the same tendency noticed for *MEG3* (Figure 3F). Therefore, the upregulation of the *DLK1/DIO3* locus appears to be associated with chromatin opening at the DLK1-WRE site in human HB with *CTNNB1* mutations.

β-Catenin/TCF-4 binding to DLK1-WRE is required for its optimal enhancer activity

To decipher if the DLK1-WRE site is the key region underlying β-catenin regulation, we designed two small guide RNAs (sgRNAs) to remove the DLK1-WRE site by CRISPR-Cas9 editing (DLK1/DIO3$^{\Delta WRE}$) without potential off-targets (Figure S5A). Then, sgRNAs were integrated into plasmids containing the saCas9 sequence and inverted terminal repeats, allowing *in vivo* editing using AAV8 particles.[28] Once subcloned, these constructs were

CTNNB1 exon 3 deletion. (C) Correlation between *RIAN*, *MIRG*, *DIO3OS*, *DIO3*, *MEG3*, miR-411, and miR-136 expressions in cohort 1. (D) *RIAN*, *RTL-1*, and *MEG3* expression determined by RT-qPCR in primary (N = 83) and recurrent HB (N = 17) versus non-tumor liver (NTL) (N = 100, cohort 2). (E) Expression of *DIO3OS*, *MEG3*, and *RIAN* determined by RT-qPCR in the different subgroups of HB: embryonal (green), fetal hepatocytic 1 (pink), fetal hepatocytic 2 (yellow), and mesenchymal (purple). (F) Expression of *RIAN*, *DIO3OS*, and *MEG3* determined by RT-qPCR in primary HB with *CTNNB1* mutations (CTNNB1^{mut}, N = 76) or with intact *CTNNB1* (CTNNB1^{WT}, N = 7). *p < 0.05, ***p < 0.005, ****p < 0.001; ns, non-significant (Kruskal-Wallis),with error bars representing SEM.

Figure 4. DLK1-WRE editing affects Apc$^{\Delta hep}$ hepatocyte proliferation through inhibition of mitosis and cytokinesis regulators

(A) Percentage of Ki-67+ hepatocytes in WT, Apc$^{\Delta hep}$-Rosa26, and Apc$^{\Delta hep}$-DLK1/DIO3$^{\Delta WRE}$ livers. (B) Percentage of liver to body weight ratio in WT, Apc$^{\Delta hep}$-Rosa26, and Apc$^{\Delta hep}$-DLK1/DIO3$^{\Delta WRE}$ livers. (C) Expression of *Top2a*, *Kif20b*, *Nuf2*, and *Nusap1* in Apc$^{\Delta hep}$-DLK1/DIO3$^{\Delta WRE}$ hepatocytes relative to Apc$^{\Delta hep}$-Rosa26

(legend continued on next page)

validated in the murine Hepa1-6 cell line with *Ctnnb1* mutation: DNA editing in one stable clone (Figure S5A) was successfully associated with a decrease in *Rian*, *Mirg*, *Meg3*, and *Rtl1* expression (Figure S5B), as well as downregulation in DLK1 protein level (Figure S5C).

Once validated, we genetically edited the DLK1-WRE site *in vivo* with AAV8 constructs in $Apc^{\Delta hep}$ mice, with the inactive Rosa26 locus as controls (Figure S1A). As expected, DLK1-WRE editing was only detected in $Apc^{\Delta hep}$-$DLK1/DIO3^{\Delta WRE}$ hepatocytes but not in non-parenchymal cells (Figures S5D and S5E). This resulted in a drastic decrease in all RNAs produced from the *Dlk1/Dio3* locus in both RNA-seq and RT-qPCR experiments in $Apc^{\Delta hep}$-$DLK1/DIO3^{\Delta WRE}$ hepatocytes (Tables S5 and S6; Figure S5F), with no impact in WT livers (Figure S5G). Additionally, impairment of TCF-4 binding at the DLK1-WRE site in $Apc^{\Delta hep}$-$DLK1/DIO3^{\Delta WRE}$ hepatocytes (Figure 2F) was associated with a decrease in both H3K4me1 and H3K27ac marks (Figure 2G) and less chromatin opening (Figure 2H). The 3C experiments in $Apc^{\Delta hep}$-$DLK1/DIO3^{\Delta WRE}$ hepatocytes showed that the 3D-chromatin organization at the DLK1-WRE site got closer to that detected in WT hepatocytes: interactions between the DLK1-WRE site and the site 2 were reinforced, while looping with the site 3 containing the Ig-DMR and the site 6 near miR-136 was lost (pink triangles in Figure 2E).

Altogether, DLK1-WRE site suppression by CRISPR-Cas9 editing *in vivo* indicates that TCF-4/β-catenin binding at the DLK1-WRE site drives its enhancer activity and the subsequent upregulation of the entire *Dlk1/Dio3* locus.

DLK1-WRE site editing in $Apc^{\Delta hep}$ hepatocytes primarily affects regulators of mitotic entry and progression

Phenotypically, $Apc^{\Delta hep}$-$DLK1/DIO3^{\Delta WRE}$ livers demonstrated significant decrease in the number of Ki-67+ hepatocytes (Figure 4A) associated with a reduced hepatomegaly[20] (Figure 4B) compared to $Apc^{\Delta hep}$-Rosa26 controls. Comparisons of RNA-seq data from $Apc^{\Delta hep}$-$DLK1/DIO3^{\Delta WRE}$ versus $Apc^{\Delta hep}$-Rosa26 hepatocytes showed that, among the top 50 most significantly dysregulated genes, several genes implicated in cell proliferation and division were downregulated: *Ccna2*, *Ccnb1*, *Kif20a*, *Kif20b*, *Ckap2*, *Top2a*, *Cdc2*, *Racgap1*, *Kif4a*, *Hmmr*, *Nusap1*, and *Nuf2* (Table S7, some of which are confirmed by RT-qPCR in Figure 4C). These genes were upregulated in $Apc^{\Delta hep}$ hepatocytes compared to WT hepatocytes (Table S8). Comparing $Apc^{\Delta hep}$-$DLK1/DIO3^{\Delta WRE}$ versus $Apc^{\Delta hep}$-Rosa26 hepatocytes, Gene Ontology identified genes related to microtubule cytoskeleton, mitotic spindle, cytokinesin, and cyclin B1/CDK1 complex (Figures 4D and 4E) and STRING analysis (https://string-db.org/) unveiled a hub of genes related to mitotic sister chromatid segregation and cyclin-associated events during G2/M transition (Figure 4F).

FoxM1, a typical proliferation-associated transcription factor, is known to regulate the expression of genes involved in G2/M-transition and M-phase progression,[29] including *Kif20a*, *Ccna2*, *Cdc2*, or *Cenpf*. Therefore, we hypothesized that FoxM1 might be the keystone linking the *DLK1/DIO3* locus to proliferative actors. While we did not observe any difference in *Foxm1* expression (Figure 5A) or nuclear localization (Figure 5B) between all conditions, we noticed that FoxM1 binding was decreased at *Ccna2*, *Kif20a*, and *Cdc2* promoters in $Apc^{\Delta hep}$-$DLK1/DIO3^{\Delta WRE}$ hepatocytes compared to $Apc^{\Delta hep}$-Rosa26 hepatocytes (Figure 5C). We hypothesized that one lncRNA within the locus, either *Meg3*, *Rian*, or *Mirg*, could act as a guide for FoxM1 at these specific promoter regions. RNA immunoprecipitation (RIP) experiments showed that *Meg3* was co-immunoprecipitated with FoxM1 in $Apc^{\Delta hep}$-Rosa26 hepatocytes, while this association was undetectable in $Apc^{\Delta hep}$-$DLK1/DIO3^{\Delta WRE}$ hepatocytes (Figure 5D).

Altogether, these results indicate that the upregulation of the *DLK1/DIO3* locus, driven by the β-catenin-dependent DLK1-WRE enhancer, favors FoxM1-mediated cell proliferation in hepatocytes.

DLK1-WRE site editing impairs $Apc^{\Delta hep}$ HB and HCC growth through cell-autonomous mechanisms and immune remodeling

We studied the effect of DLK1-WRE editing on $Apc^{\Delta hep}$ and $\beta\text{-catenin}^{\Delta exon3}$ tumor development (Figures S1B and S1C). At sacrifice, we obtained 50% HCC- and 50% HB-like tumors (Figures 6A and S6A). Around 50% of tumors were not edited at the DLK1-WRE site as an expected consequence of the probability rule for concomitant invalidation of both *Apc* and the DLK1-WRE site in the same hepatocyte ($Apc^{\Delta hep}$-$DLK1/DIO3^{WT}$) (Figures 6B and S6B). Retrospective analysis of tumor areas obtained by ultrasonography follow-up[21,22] showed that HB-like tumor growth was reduced for $Apc^{\Delta hep}$-$DLK1/DIO3^{\Delta WRE}$ subgroups (Figure 6C, pink plots) compared to $Apc^{\Delta hep}$-Rosa26 (Figure 6C, blue plots) and $Apc^{\Delta hep}$-$DLK1/DIO3^{WT}$ (Figure 6C, green plots) HB-like tumors.

The slower growth of $Apc^{\Delta hep}$-$DLK1/DIO3^{\Delta WRE}$ HB-like tumors was associated with less Ki-67+ staining (Figure 6D). *Rian*, *Mirg*, *Mki67*, *Ccna2*, *Nuf2*, *Top2a*, *Kif20b*, *Ckap2*, *Cenpf*, and *Nusap1* were underexpressed in $Apc^{\Delta hep}$-$DLK1/DIO3^{\Delta WRE}$ HB-like tumors compared to $Apc^{\Delta hep-}$Rosa26 HB-like tumors and, in most cases, compared to $Apc^{\Delta hep}$-$DLK1/DIO3^{WT}$ HB-like tumors (Figures 6E and 6F). Moreover, *Axin2* was also decreased in $Apc^{\Delta hep}$-$DLK1/DIO3^{\Delta WRE}$ HB-like tumors compared to $Apc^{\Delta hep-}$Rosa26 HB-like tumors

hepatocytes. (D–F) RNA-seq analysis on $Apc^{\Delta hep-}DLK1/DIO3^{\Delta WRE}$ and $Apc^{\Delta hep}$-Rosa26 hepatocytes. (D) The histograms summarize ratio obtained with gene set enrichment analysis (GSEA) between the number of genes in the intersection of the query set with a set from MSigDB (k/K), with p value and FDR q-values for each item. (E) Schematic representation of the most significantly deregulated RNAs. (F) Main hub obtained by STRING analysis. *p < 0.05, **p < 0.01, ****p < 0.001; ns, non-significant (Mann-Whitney), with error bars representing SEM.

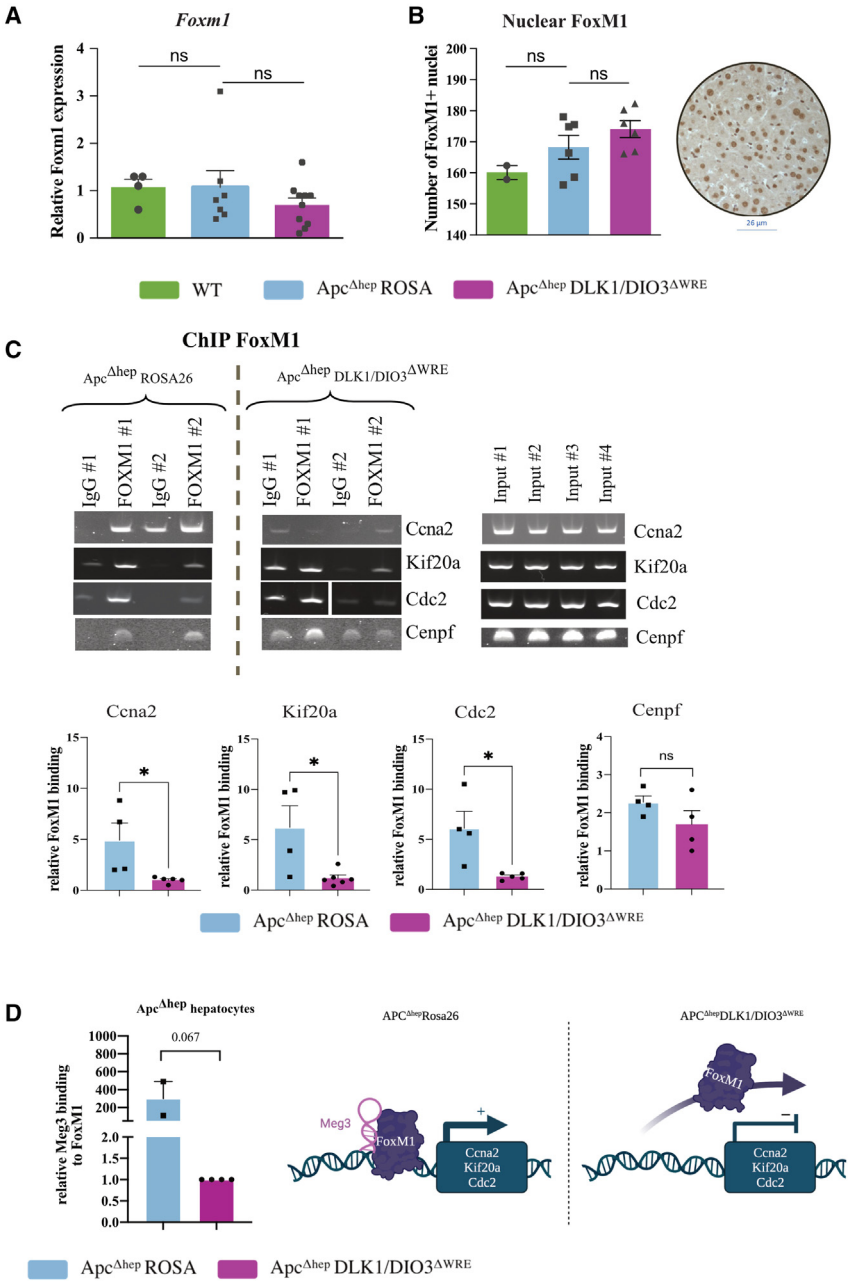

Figure 5. DLK1-WRE editing impairs FoxM1 binding at *Ccna2*, *Kif20a*, and *Cdc2* promoters

(A) RT-qPCR analysis of *Foxm1* expression in Apc$^{\Delta hep}$-Rosa26 and Apc$^{\Delta hep}$-DLK1/DIO3$^{\Delta WRE}$ hepatocytes compared to WT hepatocytes. (B) Number of Foxm1+ nuclei in IHC. (C) Representative images of ChIP-PCR targeting FoxM1 at *Ccna2*, *Kif20a*, *Cdc2*, and *Cenpf* promoters compared to isotype control in Apc$^{\Delta hep}$-Rosa26 and Apc$^{\Delta hep}$-DLK1/DIO3$^{\Delta WRE}$ hepatocytes and inputs (#1 and 2 for Apc$^{\Delta hep}$-Rosa26 hepatocytes, #3 and 4 for Apc$^{\Delta hep}$-DLK1/DIO3$^{\Delta WRE}$hepatocytes); the lower panel represents the PCR band quantification with ImageJ of all ChIP experiments against FoxM1 relative to isotype control. For the cdc2 promoter in Apc$^{\Delta hep}$-DLK1/DIO3$^{\Delta WRE}$ hepatocytes, the cropped images are for two different mice analyzed on two gels with the same conditions of exposure. (D) Quantification of *Meg3* RNA co-immunoprecipitated with FoxM1 in RIP-qPCR in Apc$^{\Delta hep}$-DLK1/DIO3$^{\Delta WRE}$ (n = 4) compared to Apc$^{\Delta hep}$-Rosa26 hepatocytes (n = 2); data are represented as the relative binding compared to 18S. Figure made with BioRender. *p < 0.05, **p < 0.01; ns, non-significant (Kruskal-Wallis or Mann-Whitney), with error bars representing SEM.

(Figure 6F), which probably reflects decreased β-catenin signaling in these tumors.

In both Apc$^{\Delta hep}$ and β-catenin$^{\Delta exon3}$ HCC (Figures S6C and S7B, respectively), we observed a decrease in tumor growth for DLK1/DIO3$^{\Delta WRE}$ HCC (pink/purple plots) compared to Rosa26 HCC (blue plots). DLK1-WRE editing was associated with lower Ki-67 staining (Figure S7C) and decreased *Mki67*, *Top2a*, and *Kif20b* expression levels (Figure S7D) in β-catenin$^{\Delta exon3}$-DLK1/DIO3$^{\Delta WRE}$ HCC in agreement with the significant reductions in *Rian*, *Mirg*, and miR-127 expressions (Figure S7E). In Apc$^{\Delta hep}$-DLK1/DIO3$^{\Delta WRE}$ HCC, DLK1-WRE editing in the tumors tended to reduce *Rian* and *Mirg* expression (Figure S6D) in a non-significant manner, probably because of the higher basal level observed in *Dlk1/Dio3* locus expression in Apc$^{\Delta hep}$ HCC (Figures 1D and 1E). This mild repression of the *Dlk1/Dio3* locus was associated with comparable number of Ki67+ cells (Figure S6E) and *Mki67*, *Ccna2*, *Top2a*, and *Kif20a* expression levels (Figure S6F). However, Apc$^{\Delta hep}$-DLK1/DIO3^{WT} tumor size and growth were significantly impaired compared to Apc$^{\Delta hep}$-Rosa26 tumors (Figure S6C, green plot). Unfortunately, we could not obtain β-catenin$^{\Delta exon3}$-DLK1/DIO3^{WT} HCC to confirm this observation, as a consequence of the concomitant injection and subsequent co-entry of CRISPR-Cas9 constructs into hepatocytes. By comparing Apc$^{\Delta hep}$ and β-catenin$^{\Delta exon3}$ models, we nevertheless observed significant differences in *Mki67*, *Ccna2*, and *Top2a* expression, which were drastically higher in β-catenin$^{\Delta exon3}$ non-tumor tissues compared to Apc$^{\Delta hep}$ non-tumor tissues (Figure S7F). This could suggest that the proliferative index of the adjacent non-tumor tissue could also influence β-catenin-driven HCC growth and efficacy of DLK1-WRE editing.

Next, since oncogenic β-catenin is known to trigger an inflammatory response associated with a significant infiltration of immune cells in Apc$^{\Delta hep}$ livers,[30] we analyzed immune cell proportions by flow

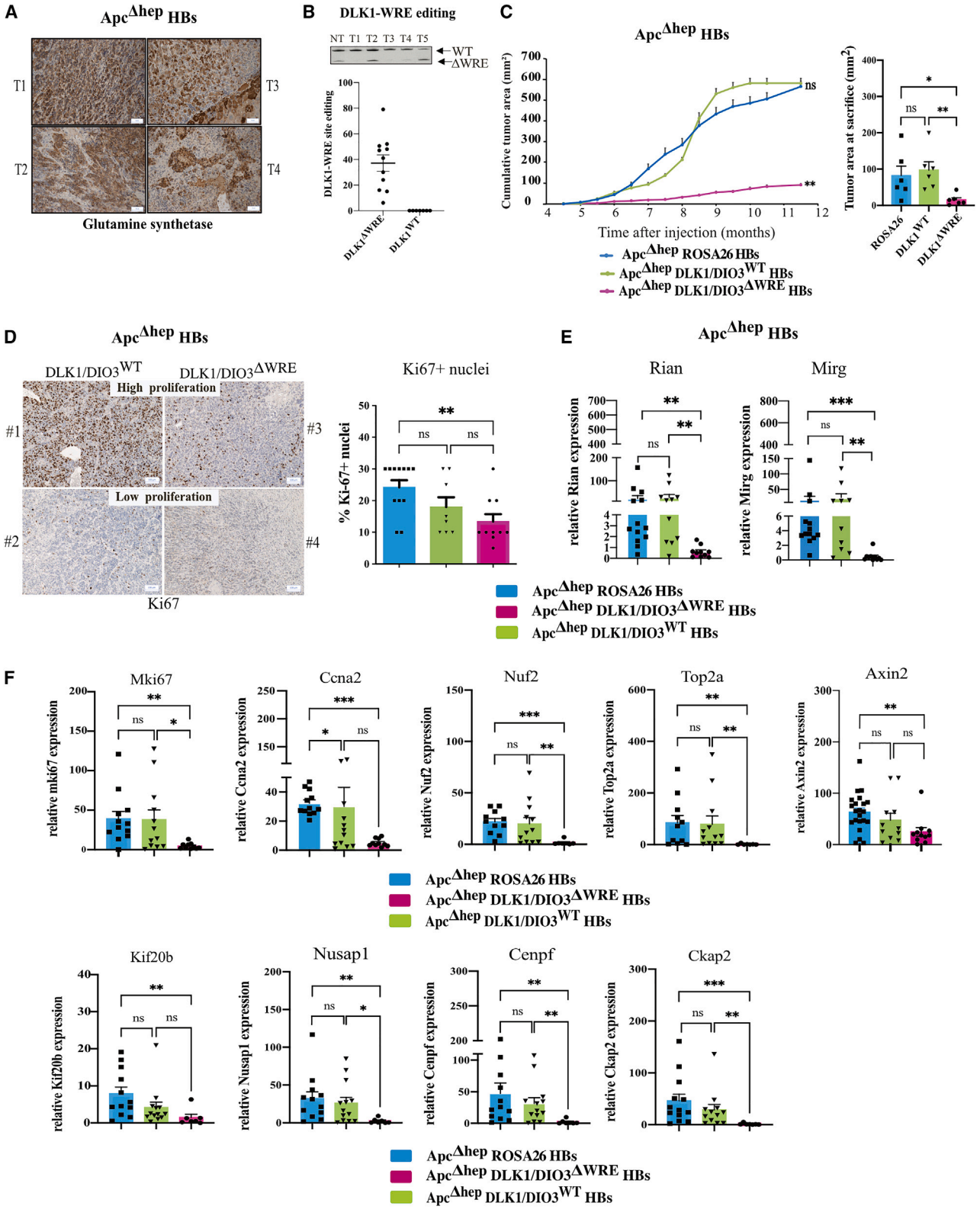

(legend on next page)

cytometry. In both Apc$^{\Delta hep}$ and β-catenin$^{\Delta exon3}$ DLK1/DIO3$^{\Delta WRE}$ tumors, monocyte infiltration was reduced as compared to Rosa-26 controls (Figures S8A and S8C), in association with decreased expression in *Ccl2*, *Ccl5*, and *Csf1* mRNAs, encoding three chemokines essential for monocyte recruitment (Figures S8B and S8D). This suggests that the immune response fostered by oncogenic β-catenin signaling could arise in part downstream of the activation of the *DLK1/DIO3* locus and potentially contribute to its tumor-promoting effect.

Altogether, our results show that β-catenin-driven HB growth is mainly dependent on the level of activation of the *DLK1/DIO3* locus in the tumor itself, while β-catenin-driven HCC growth seems to be affected by the *DLK1/DIO3* level, not only in the tumor but also in the surrounding tissue. They also point to the activation of the *DLK1/DIO3* locus as a key intermediate in the oncogenic β-catenin-dependent infiltration of monocytes in the tumors.

Editing of the DLK1-WRE site impairs the pro-tumorigenic capacities of human and mouse hepatic cancer cell lines harboring β-catenin mutations

Finally, we investigated the impact of DLK1-WRE editing in transformed cell lines from mouse and human hepatic cancers harboring β-catenin mutations. The DLK1/DIO3$^{\Delta WRE}$ Hepa1-6 clones, characterized in Figures S5A–S5C, were less proliferative than the Rosa26 clones (Figure 7A). This was accompanied by a significant increase in the number of DLK1/DIO3$^{\Delta WRE}$ cells in G2/M phase (Figure 7B) together with a decrease in cyclin B1 protein level, a protein required for mitotic initiation (Figure 7C). As observed in Apc$^{\Delta hep}$-DLK1/DIO3$^{\Delta WRE}$ hepatocytes (Figure 5D), RIP experiments showed that *Meg3* co-immunoprecipitation with FoxM1 was decreased in Hepa1-6-DLK1/DIO3$^{\Delta WRE}$ clones compared to Hepa1-6-Rosa26 clones (Figure 7D). Consistent with *in vitro* data, Hepa1-6-DLK1/DIO3$^{\Delta WRE}$ clones also exhibited decreased tumorigenic capacity compared to Hepa1-6-Rosa26 clones after subcutaneous allografting into Nu/Nu mice. Tumor progression was significantly slower for Hepa1-6-DLK1/DIO3$^{\Delta WRE}$ clones (Figure 7E) with 2.6-fold lower mean tumor volume and 4-fold lower weight at the time of sacrifice (Figure 7F). Impaired DLK1/DIO3$^{\Delta WRE}$ tumor progression in Nu/Nu mice was consistent with less Ki-67+ staining (Figure 7G) and more cells harboring cleaved caspase-3 (Figure 7H) compared to Rosa26 tumors. According to Targetscan and Dianalab algorithms, FADD, a pro-apoptotic actor, is a potential target of miR-134 produced within the *DLK1/DIO3* locus. We found that Fadd was increased in DLK1/DIO3$^{\Delta WRE}$ Hepa1-6 tumors at both the mRNA and protein level (Figures 7I and 7J), and could favor caspase-3 cleavage.

The active DLK1-WRE site being conserved in human hepatic cell lines and HB tumors (Figures 3A and S5H), we also generated DLK1/DIO3$^{\Delta WRE}$ clones from the Huh6 cell line, a human HB cell line with a *CTNNB1* mutation (Figure S5H). Editing of the DLK1-WRE site led to reduced expression of *RIAN*, *MIRG*, *MEG3*, and *RTL-1* (Figure S5I). Proliferation of DLK1/DIO3$^{\Delta WRE}$ Huh6 clones was slower than that of control clones (Figure 8A). In line with this, a significant increase in the number of DLK1/DIO3$^{\Delta WRE}$ cells in G2/M phase was noticed (Figure 8B). DLK1/DIO3$^{\Delta WRE}$ clones had a significantly reduced capacity to grow as spheroids (Figure 8C). *In vivo*, DLK1/DIO3$^{\Delta WRE}$ Huh6 clones exhibited decreased tumorigenic capacity compared to control clones after subcutaneous xenografting into Nu/Nu mice (Figure 8D). A 4-fold lower mean tumor volume and weight were observed at sacrifice (Figures 8D and 8E). DLK1/DIO3$^{\Delta WRE}$ Huh6 tumors displayed a reduced number of Ki67+ cells (Figure 8F) and decreased *MKI67* expression (Figure 8G). Importantly, as previously observed in mouse Apc$^{\Delta hep}$ hepatocytes (Figure 5C), FOXM1 was found to bind *CCNA2*, *CDC2*, and *KIF20A* promoters in human Huh6 clones (Figure 8H, blue squares) but was not recruited in DLK1/DIO3$^{\Delta WRE}$ Huh6 clones (Figure 8H, pink dots). DLK1/DIO3$^{\Delta WRE}$ Huh6 tumors also displayed a higher number of cells harboring cleaved caspase-3 (Figure 8I) and increased FADD mRNA and protein levels (Figures 8J and 8K). In both DLK1/DIO3$^{\Delta WRE}$ Hepa1-6 (Figure 7K) and Huh6 grafted tumors (Figure 8L), *GLUL* expression was decreased, in agreement with inhibition of β-catenin signaling in DLK1/DIO3$^{\Delta WRE}$ tumors, as previously noticed for mouse HB-like tumors (Figure 6F).

In conclusion, the *DLK1/DIO3* locus contributes to the pro-tumorigenic capacities of transformed human hepatic cancer cells harboring β-catenin mutations by enhancing their proliferation through the FOXM1 axis and by decreasing FADD-dependent apoptotic programs both *in vitro* and *in vivo*.

DISCUSSION

Imprinted loci play major roles in cellular plasticity and cell reprogramming during cancer. More particularly, the *DLK1/DIO3* locus, also known as the 14q32.2 cluster, is crucial for cell proliferation and metabolic adaptation in the liver.[13] In human and mouse HB, we found that RNAs within the *DLK1/DIO3* locus are highly expressed and correlated with oncogenic activation of β-catenin,[3,31] as reported by others.[18] Here, we have identified a regulatory site, existing in mouse and human, responsible for the *DLK1/DIO3* locus induction driven by oncogenic TCF-4/β-catenin complexes and unveiled its functional impact on cell proliferation and apoptosis

Figure 6. DLK1-WRE site editing slows tumor growth of Apc$^{\Delta hep}$ HB through decreased expression of mitotic entry regulators

(A) Examples of GS staining of Apc$^{\Delta hep}$ HB showing a heterogeneous staining with many stromal cells; HB cells losing several metabolic features of mature hepatocytes express low level of GS compared to Apc$^{\Delta hep}$ HCC cells. (B) Analysis of tumor editing by PCR band quantification with ImageJ in Apc$^{\Delta hep}$ HB. The upper panel is a representative image obtained from NT tissue and tumors (T). (C) Progression of cumulative tumor areas in Apc$^{\Delta hep}$-DLK1/DIO3$^{\Delta WRE}$ HB and Apc$^{\Delta hep}$-DLK1/DIO3^{WT} HB compared to Apc$^{\Delta hep}$-Rosa26 HB with cumulative area at sacrifice indicated in the right panel. (D) Representative images of Ki-67 staining on Apc$^{\Delta hep}$ HB with high or low proliferation rate (left panel) and quantification of Ki-67+ hepatocytes in percentage for all tumors (right panel). (E) RT-qPCR analysis of *Rian* and *Mirg* in Apc$^{\Delta hep}$ HB compared to their NT tissues. (F) RT-qPCR analysis of *Mki67*, *Ccna2*, *Nuf2*, *Top2a*, *Axin2*, *Kif20b*, *Nusap1*, *Cenpf*, and *Ckap2* relative to their NT tissues. *$p < 0.05$, **$p < 0.01$, ***$p < 0.005$, ****$p < 0.001$; ns, non-significant (Kruskal-Wallis), with error bars representing SEM.

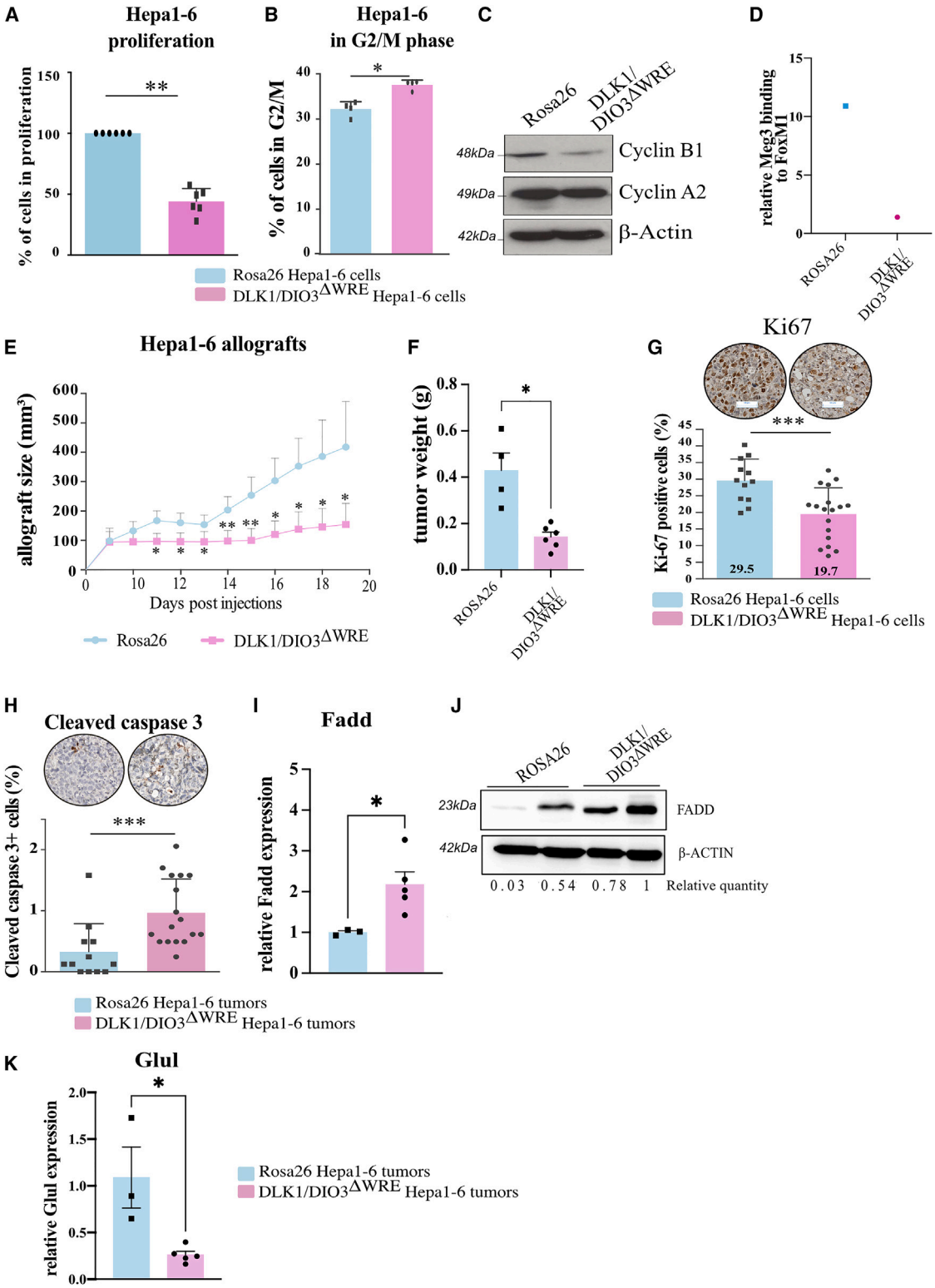

(legend on next page)

(Figure S9). We have also shown that dysregulation of the *Dlk1/Dio3* locus occurs in mouse HCCs emerging from healthy livers. Importantly, we have demonstrated that part of the oncogenic role of the *DLK1/DIO3* locus involves the DLK1-WRE enhancer site *in vivo*. Altogether, our work provides strong arguments for the therapeutic benefit of a targeted repression of the DLK1-WRE enhancer.

In our study, we have identified the regulatory region activated in the case of sustained β-catenin activation during the very early steps of liver tumorigenesis and determined how this region promotes *DLK1/DIO3* locus transcription. This transcriptional regulation requires the binding of oncogenic β-catenin/TCF-4 complexes at the DLK1-WRE site, which then becomes an active enhancer. This site is also engaged in chromatin remodeling and long-range chromatin interactions to bridge the enhancer region with other regulatory sites at the Ig-DMR and in downstream regions. This DNA looping role for β-catenin/TCF-4 complexes echoes two works published by Yochum et al. showing that β-catenin coordinates chromatin looping at an enhancer site upstream of MYC, a canonical β-catenin target in colon cancer.[32,33] Furthermore, this regulatory mechanism is also reminiscent of chromatin looping and enhancer-promoter bridging as a way to escape silencing for the imprinted *DLK1/DIO3* locus.[34] To determine the allele of origin for the regulatory functions that we unveiled at the DLK1-WRE site, we needed to generate hybrids of our transgenic mice. Nevertheless, we did not find any change in DNA methylation status at the Ig-DMR region in $Apc^{\Delta hep}$ hepatocytes, which is rather in favor of an absence of imprinting loss.

Besides increasing knowledge on the regulation of the *DLK1/DIO3* locus, our editing strategy has also deciphered the pro-tumorigenic events subsequent to its activation by β-catenin signaling. Using a CRISPR-Cas9 strategy in mouse, we showed that editing of the DLK1-WRE site inhibited HB and HCC growth in healthy livers. Nevertheless, the antitumor activity of DLK1-WRE editing was the strongest in $Apc^{\Delta hep}$ HB-like tumors. We also observed a decrease in HCC growth, notably in β-$catenin^{\Delta exon3}$ HCC with moderate activation of the *Dlk1/Dio3* locus. In $Apc^{\Delta hep}$ HCC, it appears that tumor growth is highly dependent on *Dlk1/Dio3* locus expression in the tumor microenvironment: inhibition of tumor growth of $Apc^{\Delta hep}$-$DLK1/DIO3^{WT}$ HCC is similar to that of $Apc^{\Delta hep}$-$DLK1/DIO3^{\Delta WRE}$ HCC, arguing that an impairment of the *DLK1/DIO3* locus in non-tumor tissues could also modulate HCC progression. HCC is the paradigm of inflammation-associated cancer emerging in cirrhotic livers in 80% of cases. The *DLK1/DIO3* locus expression has been found to be upregulated in response to several types of stress, particularly in hepatocytes under metabolic disorders[35] and lipid overload.[36]

We have exploited public RNA-seq datasets generated on samples from patients with diseased livers at high risk of HCC (GSE126848 and GSE142530). Interestingly, we found that the expression of *RTL1*, within the locus, and *AXIN2*, a canonical target of β-catenin, was upregulated during alcoholic hepatitis and metabolic dysfunction-associated steatohepatitis (MASH). This presumes an activation of β-catenin signaling in diseased livers, as reported by other studies showing that *CTNNB*1-mutated HCCs are significantly over-represented under MASH context.[37,38] These results are also in agreement with data obtained by others in db/db and ob/ob mice,[36,39] as well as data generated in our lab with mice fed with choline-deficient diet and methionine-choline-deficient diets, showing an increased expression in *Mirg*, *Rian*, and *Meg3* (unpublished data).

Besides their roles in hepatocytes, the dysregulation of ncRNAs within the locus has also been reported in immune cells during inflammation, particularly in macrophages.[40,41] Here, we exemplified that DLK1-WRE editing in both $Apc^{\Delta hep}$ and β-$catenin^{\Delta exon3}$ tumors impaired monocyte infiltration and expression of *Ccl2*, *Ccl5*, and *Csf1* encoding chemokines essential for monocyte recruitment. This could open new perspectives regarding the role played by the locus in the control of immune cell populations, with the underlying molecular mechanisms remaining to be deciphered. This also reinforces the interest to impair locus expression during chronic liver diseases preceding HCC.

Our data obtained on $DLK1/DIO3^{\Delta WRE}$ hepatocytes and transformed hepatic cell lines revealed that inhibition of cell proliferation and tumor progression was associated with a decrease in the mRNA levels of several actors involved in cytokinesis and G2/M phase, the cell phase during which the levels of β-catenin rise to a peak.[42] Interestingly, a hub between cell cycle actors and miRNAs within the *DLK1/DIO3* locus has also been inferred by bioinformatics analysis of HB datasets.[43] Here, our study supports that the proliferative impact of the *DLK1/DIO3* locus in preneoplastic hepatocytes is dependent on the β-catenin-driven DLK1-WRE enhancer and the subsequent redistribution of FoxM1 at the promoters of cell cycle actors. *Meg3* appears as a potential guiding partner for FoxM1 at these promoters to regulate their transcription. FOXM1 is involved in the progression of several cancers, including HB,[44] and compounds inhibiting FOXM1 have recently demonstrated encouraging antitumor activities.[45] This could open new innovative treatment strategies against FOXM1 as an alternative target for the treatment of *CTNNB1*-mutated cancers.

Altogether, our results unveil how a sustained activation of β-catenin signaling can remodel the epigenetic and chromatin landscape of one of its key oncogenic targets with a subsequent effect on proliferative

Figure 7. DLK1-WRE site editing impairs the pro-tumorigenic capacities of murine hepatoma Hepa1-6 cells mutated for *Ctnnb1*

(A–D) Analysis of $DLK1/DIO3^{\Delta WRE}$ Hepa1-6 clones versus Rosa26 control clones. Proliferation rate at 48 h (A); percentage of cells in G2/M phase determined by flow cytometry (B); cyclin B1 and A2 protein level determined by western blot (C); representative quantification of *Meg3* RNA co-immunoprecipitated with FoxM1 in RIP-qPCR (n = 2) with data represented as the relative binding compared to 18S (D). (E–K) Analysis of $DLK1/DIO3^{\Delta WRE}$ Hepa1-6 tumors versus Rosa26 tumors. Tumor volumes measured every 2 days (E) and tumor weights at sacrifice (F); percentage of Ki67+ tumor cells (G); percentage of tumor cells with cleaved caspase-3 (H); *Fadd* level determined by RT-qPCR (I); FADD protein level determined by western blot (J); *Glul* expression determined by RT-qPCR (K). *p < 0.05, **p < 0.01, ***p < 0.005, ****p < 0.0001 (Mann-Whitney),with error bars representing SEM.

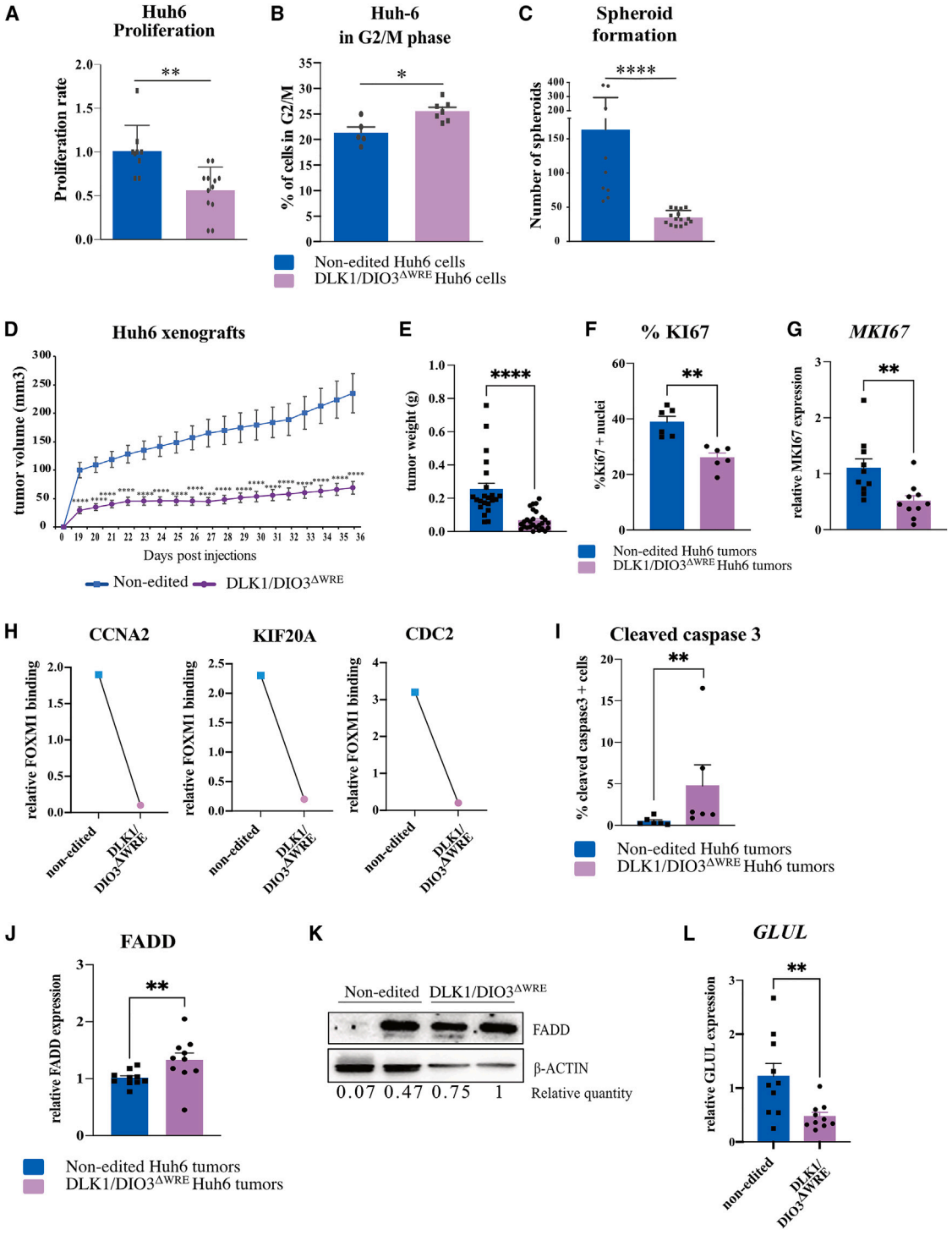

Figure 8. DLK1-WRE site editing impairs the pro-tumorigenic capacities of human Huh6 HB cells mutated for *CTNNB1*

(A–C) Analysis of DLK1/DIO3$^{\Delta WRE}$ Huh6 clones versus non-edited clones. Proliferation rate at 48 h (A); percentage of cells in G2/M phase determined by flow cytometry (B); number of spheroids (C). (D–L) Analysis of DLK1/DIO3$^{\Delta WRE}$ Huh6 tumors versus non-edited tumors. Tumor volumes measured every 2 days (D); tumor weights at sacrifice (E); percentage of Ki67+ tumor cells (F); *MKI67* level determined by RT-qPCR (G); representative FOXM1 binding at *CCNA2*, *KIF20A*, and *CDC2* promoters normalized to isotype control in ChIP-qPCR experiments (n = 2) (H); percentage of tumor cells with cleaved caspase-3 (I); *FADD* mRNA level determined by RT-qPCR (J); FADD protein level determined by western blot (K); *GLUL* expression determined by RT-qPCR (L). *p < 0.05, **p < 0.01, ***p < 0.005, ****p < 0.0001 (Mann-Whitney)with error bars representing SEM

gene signatures. We put forward the idea that targeting the DLK1-WRE site represents a potent strategy to specifically repress the *DLK1/DIO3* locus in liver tumors harboring β-catenin mutations. Regarding the crucial role of β-catenin in tissue homeostasis and repair after injury, many drugs targeting this pathway have failed in treatments because of their toxicities. Targeting downstream events, as we have outlined here with the *DLK1/DIO3* locus, appears as a promising option. This could be performed by gene editing therapies with zinc-finger nucleases, which gave promising results in hemophilia B (NCT02695160 ongoing). The development of *in silico* approaches to predict genome-wide off-targets will open up new horizons for gene editing therapy, which could benefit our proposed strategy against the *DLK1/DIO3* enhancer in particular in HB but also probably during chronic liver diseases and HCC.

MATERIAL AND METHODS

In vivo CRISPR-Cas9 design and gene editing analysis

sgRNAs against the DLK1-WRE site were designed as previously for β-catenin$^{\Delta Exon3}$ (Table S9).[23] DNA was extracted from edited cells, livers, and tumors and analyzed as previously (Table S9).[23] PCR products were run on E-Gel 2% for 10 min (Thermo Fisher, Waltham, MA) and bands quantified with ImageJ.

Murine models

The Apc$^{lox/lox}$ model was edited for the DLK1-WRE site with 3.6×10^{11} Vg (viral genomes) of sg2 plus 1.9×10^{11} Vg of sg5 (DLK1/DIO3$^{\Delta WRE}$) 1 month before β-catenin activation as reported elsewhere.[23] Intraperitoneal injection of 2 mg of tamoxifen (MP Biomedicals, Irvine, CA) in *Apc$^{lox/lox}$* TTR-Cre^{ERT2} mice resulted in *Apc* deletion in ≥90% of hepatocytes for preneoplastic studies 6 days post injection (pretumoral Apc$^{\Delta hep}$ model; Figure S1A).[19–21] A unique injection of 1×10^9 Vg of an Ad5-Cre-GFP adenovirus led to tumors within 4–6 months,[20] which were monitored by 2D-ultrasound (Vevo 2100, Visualsonics, Toronto, Canada), as previously published (Figure S1B).[21] The tamoxifen procedure to inactivate β-catenin in mice carrying a biallelic floxed *Ctnnb1* gene with *loxP* sites located between exons 2 and 6 and a TTR-Cre^{Tam} (βcat$^{\Delta hep}$) was reported elsewhere.[5,46,47] DEN-induced livers tumors were obtained by intraperitoneal injection of 0.25 mg of DEN (Sigma Aldrich, St. Louis, MO) in 14-day-old male mice. The HNF4α$^{\Delta hep}$ model was obtained as described earlier.[48,49]

For the β-catenin$^{\Delta Exon3}$ model, AAV8 against the DLK1-WRE site and the exon 3 of *Ctnnb1*[23] were concomitantly administered and mice were monitored as described above (Figure S1C).

Kinetic hepatocyte sorting was performed after retro-orbital injection of 1.5×10^9 particles of Ad5-Cre-GFP adenovirus, liver perfusion with collagenase as described previously,[21] and GFP sorting on an ARIA3 (BD, Franklin Lakes, NJ) (Figure S1D).

Subcutaneous allografts were performed with 2×10^6 cells on both flanks from 5-week-old female Nu/Nu nude mice as reported elsewhere.[50] All animal procedures were carried out according to French legal regulations and approved by an ethical committee (agreements 17-082, 14009, and 16420).

Human samples

All samples were recruited in accordance with European and French law and institutional ethical guidelines. For HB cohort 1 (N = 22; Table S3), RNA-seq was performed on total RNA extracted from tumoral and adjacent non-tumor tissues surgically resected from 22 patients using the *mir*Vana kit (Thermo Fisher, Waltham, MA) according to the supplier's protocol. The RNA integrity number was evaluated by Agilent 2100 Bioanalyzer. Two micrograms were used for generation of each small RNA library with an Illumina TruSeq Small RNA Sample Prep Kit according to standard protocol (Illumina, San Diego, CA). Single-read 50-nt sequencing was performed by MGX-Montpellier GenomiX platform on an Illumina HiSeq 2000 using the sequence-by-synthesis technique. Adapter sequences were trimmed from small RNA reads using the Cutadapt (version 1.4.1) tool (http://code.google.com/p/cutadapt/), retaining reads of the size 16–25 nt. Reads were then mapped to the human hairpin sequences (mirBase version 21) with Bowtie (v1.0). The number of reads mapping in the sense orientation to each hairpin in each patient was used as an input for further analysis. Data were analyzed using DESeq2 package in R studio. The miRNA expression file was loaded in format .txt to obtain a matrix with the value in i-th row corresponding to miRNA names and value in j-th column corresponding to patient samples. We followed the DESeq2 manual,[51] performed differential miRNA expression analysis (DE), and produced output files including heatmaps and tables. After the DE analysis, DESeq2 produces a set of values (base mean, log2 fold change, and adjusted p value) for each miRNA between tumoral and non-tumor samples. Once exported, our data were classified in an Excel file and analyzed with the help of miRBase and UCSC Browser (https://genome.ucsc.edu/).

For the HB cohort 2 (N = 100; Table S4), RNA-seq was performed as previously described.[3,52,53] Gene expression levels were calculated using the variance stabilizing transformation (VERSUST) and the raw count matrix. Gene-expression-based classification of HB was done as previously described.[3] Statistical analysis and data visualization were performed using R software version 3.6.1 (R Foundation for Statistical Computing, Vienna, Austria; https://www.R-project.org) and Bioconductor packages.

RNA-seq data from a collection of livers with varying degrees of non-alcoholic fatty liver disease compared with healthy livers from normal-weight individuals (GSE126848) and liver biopsies from 28 patients with alcoholic hepatitis or cirrhosis compared to healthy controls (GSE142530) were retrieved with GEO and analyzed using the R package DESeq2 (v.1.38).[51]

Cell culture

Hepatocytes were isolated 4 days after tamoxifen injection in Apc$^{lox/lox}$ TTR-Cre^{ERT2} mice and maintained at 37°C in a humidified atmosphere containing 5% CO_2 as reported elsewhere.[21] Hepa1-6 cells were obtained from the American Type Culture Collection

and Huh6 cells from C. Perret's lab.[1] They were grown in DMEM supplemented with 10% fetal bovine serum (FBS) and 50 U/mL penicillin-streptomycin at 37°C in a humidified atmosphere containing 5% CO_2 (Thermo Fisher, Waltham, MA). Stable clones were obtained following co-transfections of sgRNA- and pmax-GFP plasmids, GFP-based sorting (ARIA3), and amplification of selected clones.

Proliferation/cell cycle analysis

Cell proliferation was measured on 8,000 cells with the xCELLigence system (Agilent, Santa Clara, CA) (N = 3), as previously described.[21] Cell cycle analysis was performed on 5×10^5 synchronized cells (with 24h FBS deprivation for Huh6 cells and 10 μg/mL colchicine for Hepa1-6 cells), fixed 48 h later in PBS-20%/ethanol-80% at −20°C for 15 min and stained with FxCycle PI/RNAse solution (Thermo Fisher, Waltham, MA) for 30 min at room temperature before analysis (Fortessa, BD).

Sphere formation assay

One thousand Huh6 clones were grown during 14 days onto ultra-low-attachment six-well plates (Corning, Corning, NY) in DMEM/F12 medium supplemented with B27, 20 ng/mL epidermal growth factor (EGF), 20 ng/mL basic fibroblast growth factor (FGF), and 100 μg/mL gentamycin (Thermo Fisher, Waltham, MA) (N = 3).

RNA extraction and RT-qPCR

Levels of miRNAs and mRNAs were determined on total RNA extracted with Trizol reagent (Thermo Fisher, Waltham, MA), as previously reported (Table S9).[21]

Quantitative chromosome conformation capture (3C-qPCR)

The 3C-qPCR experiment was adapted from Braem et al. and Rebouissou et al.[26,54] and conducted on 5 million nuclei isolated from hepatocytes lysed in homogenization buffer with an Ultra-Turrax during 20 min on ice and centrifuged for 1 h at 20,000 × *g*. The 3C assays were performed with EcoRI digestion, product ligation, and secondary XbaI digestion ($N \geq 3$).[26] Sample purity and DNA content were determined with internal primers against *Gapdh* and digestion efficiency with three primer sets (Table S9). For all 3C experiments, qPCR primers used were as previously published with the anchor F16 located at the beginning of the DLK1-WRE site and thus not affected by the CRISPR-Cas9 constructs used.[55] Their efficiencies were determined on equimolar amounts of 3C-ligation products generated from BAC RPCI-23 clone 117C15 (Thermo Fisher, Waltham, MA) covering the genome segment between *DLK1* and *miR-136* genes. The 3C data were normalized to the basal interaction level using the previously published algorithm.[26]

ATAC-seq and ATAC-qPCR

The 50,000 isolated hepatocytes were transposed for 30 min in a 50 μL reaction mix containing 4.5 μL of transposase (kit #FC-121-103, Illumina, San Diego, CA) and 0.1% digitonin (adapted from Corces et al.[56]) and the initial protocol was followed after transposition[57] for ATAC-seq and ATAC-qPCR experiments (Table S9). For liver samples, omni-ATAC-seq was performed on 50,000 nuclei, isolated as for 3C assays, according to Corces et al.[58] in a 50 μL reaction mix with 2.5 μL of transposase, 0.01% digitonin, and 0.1% Tween 20 for 30 min. The following steps were according to the initial protocol.[57]

Libraries were controlled using a 2100 Bioanalyzer, and an aliquot of each library was sequenced at low depth onto a MiSeq platform to control duplicate level and estimate DNA concentration. Each library was then paired-end sequenced (2 × 100 bp) on a HiSeq instrument to get 40 million read pairs on average. As ATAC-seq libraries are composed in large part of short genomic DNA fragments, and in order to reduce costs, we sequenced our recent libraries on a Nextseq instrument (2 × 38 bp). Our analysis showed that reducing read length to 38 bp does not affect mapping efficiency. Reads were first cleaned using Trimmomatic (removing of adaptors and low-quality bases). Trimmed reads were then aligned to the mouse genome (mm9) using Bowtie2 with the parameter -X2000, and with two mismatches permitted in the seed (default value). The -X2000 option allows fragments <2 kb to align. Duplicated reads were removed with picard-tools. Resulted bam datasets were then converted to BigWig, a coverage track adapted to visualize datasets in UCSC Genome Browser or IGV. Conversion was performed using bamCoverage command from deepTools with the parameters –binSize 10 –normalizeUsing RPKM –extendReads. The parameter –normalizeUsing RPKM is used to normalize each dataset. We selected the normalization method based on reads per kilobase per million mapped reads (RPKM), which calculates the number of reads per bin/number of mapped reads (in millions). The parameter –extendReads allows the extension of reads to fragment size. The default value is estimated from the data (mean of the fragment size of all mate reads).

In human HB, Multiome approach was performed by Integragen SA (Evry, France) on matched non-tumor livers (n = 2) and HBs (n = 3) of two patients, according to the commercial Chromium Single Cell Multiome ATAC + Gene Expression protocol. We used 10X Genomics Cell Ranger ARC 2.0.0 to align snATAC-seq reads to the human genome (GrCh38/hg38) (Roehrig et al. in revision).

ChIP and RIP

ChIP was performed as previously described[21] on 25 μg of chromatin with 30 μL of protein A/G(v/v) Dynabeads with antibodies of interest (Table S10). For tumors, samples were homogenized with an Ultra-Turrax in 1% formaldehyde for 1 min. For RIP experiments, beads were reverse crosslinked before RNA isolation by Trizol (Thermo Fisher, Waltham, MA).

RNA-seq/small RNA-seq

RNA-seq and small RNA-seq were performed on 1 μg of total RNA extracted from $Apc^{\Delta hep}$-ROSA26 versus $DLK1/DIO3^{\Delta WRE}$ hepatocytes ($N \geq 4$), respectively, with TruSeq Stranded after ribodepletion and TruSeq Small RNA and sequenced with Nextseq 500 (150b) (Illumina, San Diego, CA).

Fastq files were then aligned using STAR algorithm (version 2.7.6a), on the Ensembl *Mus musculus* GRCm38 reference release 96. Reads were then counted using RSEM (v1.3.1) and the statistical analyses

on the read counts were performed with R (version 3.6.3) and the DESeq2 package (DESeq2_1.26.0) to determine the proportion of differentially expressed genes between two conditions. We used the standard DESeq2 normalization method (DESeq2's median of ratios with the DESeq function), with a pre-filter of reads and genes (reads uniquely mapped on the genome, or up to 10 different loci with a count adjustment and genes with at least 10 reads in at least three different samples). Following the package recommendations, we used the Wald test with the contrast function and the Benjamini-Hochberg false discovery rate (FDR) control procedure to identify the differentially expressed genes. R scripts and parameters are available on GitHub (https://github.com/BSGenomique/genomic-rnaseq-pipeline/releases/tag/v1.0420). For small RNA-seq data analysis, Fastq files were uploaded on Qiagen geneglobe analysis software for alignment and counting. Then, UMI matrix were used as raw data for our R and DESeq2 pipeline.

Kinetic RNA-seq was performed on HiSeq 4000 in paired end on at least three independent samples of sorted GFP+ $Apc^{\Delta hep}$ hepatocytes at day 6, 15, and 21 after injection compared to GFP− hepatocytes.

Immunostaining/*in situ* hybridization

Paraffin-embedded liver sections were treated and labeled as previously[21,23] with antibodies and probes of interest (Tables S9 and S10).

Western blot

Experiments were conducted on 20 μg of total proteins as reported elsewhere (Table S10).[21]

Flow cytometry

Livers and tumors were minced with scissors in DMEM containing collagenase IV (2.5 mg/mL, Sigma Aldrich, St. Louis, MO) and incubated for 30 min at 37°C. Cell suspensions were passed through a 100-μm filter and stained with appropriate antibodies for 30 min on ice as previously (Table S10).[59] Data were acquired on a BD LSR Fortessa flow cytometer (BD Franklin Lakes, NJ) and analyzed with FlowJo software. Absolute cell count was calculated as previously with nonfluorescent beads and expressed as a number of cells per milligram of tissue.[59]

Statistical analysis

We assessed the significance of differences between two groups of samples using Mann-Whitney tests and between three groups of samples using Kruskal-Wallis. $p < 0.05$ was considered statistically significant. For human samples, difference in gene expression levels, in two or more than two groups, was tested using Wilcoxon or Kruskal-Wallis tests, respectively. Correlation analysis was performed using Pearson r correlation when both variables were normally distributed with the assumptions of linearity and homoscedasticity or Spearman's rank-order correlation.

DATA AND CODE AVAILABILITY

All data were deposited on GEO: RNA-seq and small RNA-seq comparing $Apc^{\Delta hep}$ ROSA/DLK1/DIO3$^{\Delta WRE}$ hepatocytes on GSE206262, ATAC-seq on GSE211930, kinetic RNA-seq on GSE210482), and MeDIP-seq on GSE239777. Others have been previously published (project: PRJNA150641 in European nucleotide archive (ENA).[5,21,23]

SUPPLEMENTAL INFORMATION

Supplemental information can be found online at https://doi.org/10.1016/j.ymthe.2024.01.036.

ACKNOWLEDGMENTS

We warmly thank for their great help during this project the three platforms Cybio (Karine Bailly and Muriel Andrieu), Genomic (Franck Letourneur and Lucie Audoux), and PIV (Franck Lager, Carmen Marchiol, and Gilles Renault) from Cochin Institute. We warmly thank the animal facilities from the Cordeliers research center and from Saint-Antoine research center (Tatiana Ledent). We also thank Helene Forher-Ting from CHIC platform at Cordeliers research center and INSERM UMR 1089 for AAV production. We warmly thank Katarzina Hooks for small RNA-seq analysis of HB cohort 1, and the two laboratory banks and L2PGH labs from CNRGH for kinetic RNA-seq in mouse. We thank Pr. Zhang for the gift of AAV8-SaCas9 constructs.

This work was supported by and received recognition from the Ligue Nationale Contre le Cancer (Team labellisation), by the Institut National de la Santé et de la Recherche Médicale (INSERM), by the Plan cancer (grant CHROMALIV), the Association Française pour l'Etude du Foie (AAP 2017), the Fondation pour la Recherche Médicale (grant no. DBI20131228566), the Agence Nationale de la Recherche (DLK1-EPILIV 2018–2021), the Institut National Du Cancer (INCa Emergence 2017; grant INCa_TRANSLA_2013_209), and the charity associations Eva pour la Vie, Aidons Marina, and E.S.CA.PE. to MIRCADE team. J.S. was funded by the Université Paris Cité. C.J. was funded by the Ligue Nationale Contre le Cancer. A.R. was supported by the Fondation pour la Recherche Médicale, grant number ECO201906008977.

AUTHOR CONTRIBUTIONS

J.S., investigation, formal analysis, methodology, validation, writing – original draft; L.P., investigation, formal analysis, methodology, validation; C.J., formal analysis, investigation, validation; I.L., investigation; S.C., formal analysis; S.P., investigation; C.D.-M., investigation; C.G., investigation, methodology; A.I., investigation; E.M., investigation; C.D., investigation; S.C., investigation, methodology, formal analysis; A.R., investigation, formal analysis; K.M., formal analysis; B.S.-P., formal analysis; J.-F.D., funding acquisition; S.M-R., resources, formal analysis; T.F., methodology, formal analysis, writing – original draft; C.F.G., resources, formal analysis; J.Z.-R., resources; S.C., conceptualization, funding acquisition, supervision; A.G., investigation, formal analysis, methodology, validation, writing – original draft, conceptualization, funding acquisition, and supervision.

DECLARATION OF INTERESTS

Two patents, PCT/EP2023/053419 and EP22305162.4, have been deposited by J.S., L.P., S.C., and A.G.

REFERENCES

1. de La Coste, A., Romagnolo, B., Billuart, P., Renard, C.A., Buendia, M.A., Soubrane, O., Fabre, M., Chelly, J., Beldjord, C., Kahn, A., and Perret, C. (1998). Somatic mutations of the beta-catenin gene are frequent in mouse and human hepatocellular carcinomas. Proc. Natl. Acad. Sci. USA *95*, 8847–8851.
2. Wei, Y., Fabre, M., Branchereau, S., Gauthier, F., Perilongo, G., and Buendia, M.A. (2000). Activation of beta-catenin in epithelial and mesenchymal hepatoblastomas. Oncogene *19*, 498–504. https://doi.org/10.1038/sj.onc.1203356.
3. Hirsch, T.Z., Pilet, J., Morcrette, G., Roehrig, A., Monteiro, B.J.E., Molina, L., Bayard, Q., Trépo, E., Meunier, L., Caruso, S., et al. (2021). Integrated Genomic Analysis Identifies Driver Genes and Cisplatin-Resistant Progenitor Phenotype in Pediatric Liver Cancer. Cancer Discov. *11*, 2524–2543. https://doi.org/10.1158/2159-8290.CD-20-1809.
4. Cadigan, K.M., and Waterman, M.L. (2012). TCF/LEFs and Wnt signaling in the nucleus. Cold Spring Harb. Perspect. Biol. *4*, a007906. https://doi.org/10.1101/cshperspect.a007906.
5. Gougelet, A., Torre, C., Veber, P., Sartor, C., Bachelot, L., Denechaud, P.D., Godard, C., Moldes, M., Burnol, A.F., Dubuquoy, C., et al. (2014). T-cell factor 4 and beta-catenin chromatin occupancies pattern zonal liver metabolism in mice. Hepatology *59*, 2344–2357. https://doi.org/10.1002/hep.26924.
6. Gougelet, A., and Colnot, S. (2012). A Complex Interplay between Wnt/beta-Catenin Signalling and the Cell Cycle in the Adult Liver. Int. J. Hepatol. *2012*, 816125. https://doi.org/10.1155/2012/816125.
7. Mosimann, C., Hausmann, G., and Basler, K. (2009). Beta-catenin hits chromatin: regulation of Wnt target gene activation. Nat. Rev. Mol. Cell Biol. *10*, 276–286. https://doi.org/10.1038/nrm2654.
8. Boyault, S., Rickman, D.S., de Reyniès, A., Balabaud, C., Rebouissou, S., Jeannot, E., Hérault, A., Saric, J., Belghiti, J., Franco, D., et al. (2007). Transcriptome classification of HCC is related to gene alterations and to new therapeutic targets. Hepatology *45*, 42–52. https://doi.org/10.1002/hep.21467.
9. Nagae, G., Yamamoto, S., Fujita, M., Fujita, T., Nonaka, A., Umeda, T., Fukuda, S., Tatsuno, K., Maejima, K., Hayashi, A., et al. (2021). Genetic and epigenetic basis of hepatoblastoma diversity. Nat. Commun. *12*, 5423. https://doi.org/10.1038/s41467-021-25430-9.
10. Cairo, S., Armengol, C., De Reyniès, A., Wei, Y., Thomas, E., Renard, C.A., Goga, A., Balakrishnan, A., Semeraro, M., Gresh, L., et al. (2008). Hepatic stem-like phenotype and interplay of Wnt/beta-catenin and Myc signaling in aggressive childhood liver cancer. Cancer cell *14*, 471–484. https://doi.org/10.1016/j.ccr.2008.11.002.
11. da Rocha, S.T., Edwards, C.A., Ito, M., Ogata, T., and Ferguson-Smith, A.C. (2008). Genomic imprinting at the mammalian Dlk1-Dio3 domain. Trends Genet. *24*, 306–316. https://doi.org/10.1016/j.tig.2008.03.011.
12. Benetatos, L., Vartholomatos, G., and Hatzimichael, E. (2014). DLK1-DIO3 imprinted cluster in induced pluripotency: landscape in the mist. Cell. Mol. Life Sci. *71*, 4421–4430. https://doi.org/10.1007/s00018-014-1698-9.
13. Labialle, S., Marty, V., Bortolin-Cavaillé, M.L., Hoareau-Osman, M., Pradère, J.P., Valet, P., Martin, P.G.P., and Cavaillé, J. (2014). The miR-379/miR-410 cluster at the imprinted Dlk1-Dio3 domain controls neonatal metabolic adaptation. EMBO J. *33*, 2216–2230. https://doi.org/10.15252/embj.201387038.
14. Benetatos, L., Hatzimichael, E., Londin, E., Vartholomatos, G., Loher, P., Rigoutsos, I., and Briasoulis, E. (2013). The microRNAs within the DLK1-DIO3 genomic region: involvement in disease pathogenesis. Cell. Mol. Life Sci. *70*, 795–814. https://doi.org/10.1007/s00018-012-1080-8.
15. Huang, J., Zhang, X., Zhang, M., Zhu, J.D., Zhang, Y.L., Lin, Y., Wang, K.S., Qi, X.F., Zhang, Q., Liu, G.Z., et al. (2007). Up-regulation of DLK1 as an imprinted gene could contribute to human hepatocellular carcinoma. Carcinogenesis *28*, 1094–1103. https://doi.org/10.1093/carcin/bgl215.
16. Luk, J.M., Burchard, J., Zhang, C., Liu, A.M., Wong, K.F., Shek, F.H., Lee, N.P., Fan, S.T., Poon, R.T., Ivanovska, I., et al. (2011). DLK1-DIO3 genomic imprinted microRNA cluster at 14q32.2 defines a stemlike subtype of hepatocellular carcinoma associated with poor survival. J. Biol. Chem. *286*, 30706–30713. https://doi.org/10.1074/jbc.M111.229831.
17. Honda, S., Chatterjee, A., Leichter, A.L., Miyagi, H., Minato, M., Fujiyoshi, S., Ara, M., Kitagawa, N., Tanaka, M., Tanaka, Y., et al. (2020). A MicroRNA Cluster in the DLK1-DIO3 Imprinted Region on Chromosome 14q32.2 Is Dysregulated in Metastatic Hepatoblastomas. Front. Oncol. *10*, 513601. https://doi.org/10.3389/fonc.2020.513601.
18. Carrillo-Reixach, J., Torrens, L., Simon-Coma, M., Royo, L., Domingo-Sàbat, M., Abril-Fornaguera, J., Akers, N., Sala, M., Ragull, S., Arnal, M., et al. (2020). Epigenetic footprint enables molecular risk stratification of hepatoblastoma with clinical implications. J. Hepatol. *73*, 328–341. https://doi.org/10.1016/j.jhep.2020.03.025.
19. Benhamouche, S., Decaens, T., Godard, C., Chambrey, R., Rickman, D.S., Moinard, C., Vasseur-Cognet, M., Kuo, C.J., Kahn, A., Perret, C., and Colnot, S. (2006). Apc tumor suppressor gene is the "zonation-keeper" of mouse liver. Dev. Cell *10*, 759–770. https://doi.org/10.1016/j.devcel.2006.03.015.
20. Colnot, S., Decaens, T., Niwa-Kawakita, M., Godard, C., Hamard, G., Kahn, A., Giovannini, M., and Perret, C. (2004). Liver-targeted disruption of Apc in mice activates beta-catenin signaling and leads to hepatocellular carcinomas. Proc. Natl. Acad. Sci. USA *101*, 17216–17221. https://doi.org/10.1073/pnas.0404761101.
21. Gougelet, A., Sartor, C., Bachelot, L., Godard, C., Marchiol, C., Renault, G., Tores, F., Nitschke, P., Cavard, C., Terris, B., et al. (2016). Antitumour activity of an inhibitor of miR-34a in liver cancer with beta-catenin-mutations. Gut *65*, 1024–1034. https://doi.org/10.1136/gutjnl-2014-308969.
22. Gougelet, A., Sartor, C., Senni, N., Calderaro, J., Fartoux, L., Lequoy, M., Wendum, D., Talbot, J.N., Prignon, A., Chalaye, J., et al. (2019). Hepatocellular Carcinomas With Mutational Activation of Beta-Catenin Require Choline and Can Be Detected by Positron Emission Tomography. Gastroenterology *157*, 807–822. https://doi.org/10.1053/j.gastro.2019.05.069.
23. Loesch, R., Caruso, S., Paradis, V., Godard, C., Gougelet, A., Renault, G., Picard, S., Tanaka, I., Renoux-Martin, Y., Perret, C., et al. (2022). Deleting the beta-catenin degradation domain in mouse hepatocytes drives hepatocellular carcinoma or hepatoblastoma-like tumor growth. J. Hepatol. *77*, 424–435. https://doi.org/10.1016/j.jhep.2022.02.023.
24. Hu, S., Cao, C., Poddar, M., Delgado, E., Singh, S., Singh-Varma, A., Stolz, D.B., Bell, A., and Monga, S.P. (2023). Hepatocyte beta-catenin loss is compensated by Insulin-mTORC1 activation to promote liver regeneration. Hepatology *77*, 1593–1611. https://doi.org/10.1002/hep.32680.
25. Yin, C., Wang, P.Q., Xu, W.P., Yang, Y., Zhang, Q., Ning, B.F., Zhang, P.P., Zhou, W.P., Xie, W.F., Chen, W.S., and Zhang, X. (2013). Hepatocyte nuclear factor-4alpha reverses malignancy of hepatocellular carcinoma through regulating miR-134 in the DLK1-DIO3 region. Hepatology *58*, 1964–1976. https://doi.org/10.1002/hep.26573.
26. Braem, C., Recolin, B., Rancourt, R.C., Angiolini, C., Barthès, P., Branchu, P., Court, F., Cathala, G., Ferguson-Smith, A.C., and Forné, T. (2008). Genomic matrix attachment region and chromosome conformation capture quantitative real time PCR assays identify novel putative regulatory elements at the imprinted Dlk1/Gtl2 locus. J. Biol. Chem. *283*, 18612–18620. https://doi.org/10.1074/jbc.M801883200.
27. Llères, D., Moindrot, B., Pathak, R., Piras, V., Matelot, M., Pignard, B., Marchand, A., Poncelet, M., Perrin, A., Tellier, V., et al. (2019). CTCF modulates allele-specific sub-TAD organization and imprinted gene activity at the mouse Dlk1-Dio3 and Igf2-H19 domains. Genome Biol. *20*, 272. https://doi.org/10.1186/s13059-019-1896-8.
28. Ran, F.A., Cong, L., Yan, W.X., Scott, D.A., Gootenberg, J.S., Kriz, A.J., Zetsche, B., Shalem, O., Wu, X., Makarova, K.S., et al. (2015). In vivo genome editing using Staphylococcus aureus Cas9. Nature *520*, 186–191. https://doi.org/10.1038/nature14299.
29. Wierstra, I. (2013). FOXM1 (Forkhead box M1) in tumorigenesis: overexpression in human cancer, implication in tumorigenesis, oncogenic functions, tumor-suppressive properties, and target of anticancer therapy. Adv. Cancer Res. *119*, 191–419. https://doi.org/10.1016/B978-0-12-407190-2.00016-2.
30. Anson, M., Crain-Denoyelle, A.M., Baud, V., Chereau, F., Gougelet, A., Terris, B., Yamagoe, S., Colnot, S., Viguier, M., Perret, C., and Couty, J.P. (2012). Oncogenic beta-catenin triggers an inflammatory response that determines the aggressiveness of hepatocellular carcinoma in mice. J. Clin. Invest. *122*, 586–599. https://doi.org/10.1172/JCI43937.
31. Indersie, E., Lesjean, S., Hooks, K.B., Sagliocco, F., Ernault, T., Cairo, S., Merched-Sauvage, M., Rullier, A., Le Bail, B., Taque, S., et al. (2017). MicroRNA therapy inhibits hepatoblastoma growth in vivo by targeting beta-catenin and Wnt signaling. Hepatol. Commun. *1*, 168–183. https://doi.org/10.1002/hep4.1029.

32. Yochum, G.S., Cleland, R., and Goodman, R.H. (2008). A genome-wide screen for beta-catenin binding sites identifies a downstream enhancer element that controls c-Myc gene expression. Mol. Cell. Biol. *28*, 7368–7379. https://doi.org/10.1128/MCB.00744-08.

33. Yochum, G.S., Sherrick, C.M., Macpartlin, M., and Goodman, R.H. (2010). A beta-catenin/TCF-coordinated chromatin loop at MYC integrates 5' and 3' Wnt responsive enhancers. Proc. Natl. Acad. Sci. USA *107*, 145–150. https://doi.org/10.1073/pnas.0912294107.

34. Kota, S.K., Llères, D., Bouschet, T., Hirasawa, R., Marchand, A., Begon-Pescia, C., Sanli, I., Arnaud, P., Journot, L., Girardot, M., and Feil, R. (2014). ICR noncoding RNA expression controls imprinting and DNA replication at the Dlk1-Dio3 domain. Dev. Cell *31*, 19–33. https://doi.org/10.1016/j.devcel.2014.08.009.

35. Zhu, X., Wu, Y.B., Zhou, J., and Kang, D.M. (2016). Upregulation of lncRNA MEG3 promotes hepatic insulin resistance via increasing FoxO1 expression. Biochem. Biophys. Res. Commun. *469*, 319–325. https://doi.org/10.1016/j.bbrc.2015.11.048.

36. de Guia, R.M., Rose, A.J., Sommerfeld, A., Seibert, O., Strzoda, D., Zota, A., Feuchter, Y., Krones-Herzig, A., Sijmonsma, T., Kirilov, M., et al. (2015). microRNA-379 couples glucocorticoid hormones to dysfunctional lipid homeostasis. EMBO J. *34*, 344–360. https://doi.org/10.15252/embj.201490464.

37. Pinyol, R., Torrecilla, S., Wang, H., Montironi, C., Piqué-Gili, M., Torres-Martin, M., Wei-Qiang, L., Willoughby, C.E., Ramadori, P., Andreu-Oller, C., et al. (2021). Molecular characterisation of hepatocellular carcinoma in patients with non-alcoholic steatohepatitis. J. Hepatol. *75*, 865–878. https://doi.org/10.1016/j.jhep.2021.04.049.

38. Rebouissou, S., Franconi, A., Calderaro, J., Letouzé, E., Imbeaud, S., Pilati, C., Nault, J.C., Couchy, G., Laurent, A., Balabaud, C., et al. (2016). Genotype-phenotype correlation of CTNNB1 mutations reveals different ss-catenin activity associated with liver tumor progression. Hepatology *64*, 2047–2061. https://doi.org/10.1002/hep.28638.

39. You, L., Wang, N., Yin, D., Wang, L., Jin, F., Zhu, Y., Yuan, Q., and De, W. (2016). Downregulation of Long Noncoding RNA Meg3 Affects Insulin Synthesis and Secretion in Mouse Pancreatic Beta Cells. J. Cell. Physiol. *231*, 852–862. https://doi.org/10.1002/jcp.25175.

40. Essandoh, K., Li, Y., Huo, J., and Fan, G.C. (2016). MiRNA-Mediated Macrophage Polarization and its Potential Role in the Regulation of Inflammatory Response. Shock *46*, 122–131. https://doi.org/10.1097/SHK.0000000000000604.

41. Ying, H., Kang, Y., Zhang, H., Zhao, D., Xia, J., Lu, Z., Wang, H., Xu, F., and Shi, L. (2015). MiR-127 modulates macrophage polarization and promotes lung inflammation and injury by activating the JNK pathway. J. Immunol. *194*, 1239–1251. https://doi.org/10.4049/jimmunol.1402088.

42. Hadjihannas, M.V., Bernkopf, D.B., Brückner, M., and Behrens, J. (2012). Cell cycle control of Wnt/beta-catenin signalling by conductin/axin2 through CDC20. EMBO Rep. *13*, 347–354. https://doi.org/10.1038/embor.2012.12.

43. Chen, T., Tian, L., Chen, J., Zhao, X., Zhou, J., Guo, T., Sheng, Q., Zhu, L., Liu, J., and Lv, Z. (2021). A Comprehensive Genomic Analysis Constructs miRNA-mRNA Interaction Network in Hepatoblastoma. (2021). Front. Cell Dev. Biol. *9*, 655703. https://doi.org/10.3389/fcell.2021.655703.

44. Garnier, A., Ilmer, M., Kappler, R., and Berger, M. (2016). Therapeutic Innovations for Targeting Hepatoblastoma. Anticancer Res. *36*, 5577–5592. https://doi.org/10.21873/anticanres.11143.

45. Shukla, S., Milewski, D., Pradhan, A., Rama, N., Rice, K., Le, T., Flick, M.J., Vaz, S., Zhao, X., Setchell, K.D., et al. (2019). The FOXM1 Inhibitor RCM-1 Decreases Carcinogenesis and Nuclear beta-Catenin. Mol. Cancer Ther. *18*, 1217–1229. https://doi.org/10.1158/1535-7163.MCT-18-0709.

46. Brault, V., Moore, R., Kutsch, S., Ishibashi, M., Rowitch, D.H., McMahon, A.P., Sommer, L., Boussadia, O., and Kemler, R. (2001). Inactivation of the beta-catenin gene by Wnt1-Cre-mediated deletion results in dramatic brain malformation and failure of craniofacial development. Development *128*, 1253–1264.

47. Torre, C., Benhamouche, S., Mitchell, C., Godard, C., Veber, P., Letourneur, F., Cagnard, N., Jacques, S., Finzi, L., Perret, C., and Colnot, S. (2011). The transforming growth factor-alpha and cyclin D1 genes are direct targets of beta-catenin signaling in hepatocyte proliferation. J. Hepatol. *55*, 86–95. https://doi.org/10.1016/j.jhep.2010.10.021.

48. Hayhurst, G.P., Lee, Y.H., Lambert, G., Ward, J.M., and Gonzalez, F.J. (2001). Hepatocyte nuclear factor 4alpha (nuclear receptor 2A1) is essential for maintenance of hepatic gene expression and lipid homeostasis. Mol. Cell. Biol. *21*, 1393–1403. https://doi.org/10.1128/MCB.21.4.1393-1403.2001.

49. Sartor, C., Bachelot, L., Godard, C., Lager, F., Renault, G., Gonzalez, F.J., Perret, C., Gougelet, A., and Colnot, S. (2019). The concomitant loss of APC and HNF4alpha in adult hepatocytes does not contribute to hepatocarcinogenesis driven by beta-catenin activation. Liver Int. *39*, 727–739. https://doi.org/10.1111/liv.14068.

50. Blivet-Van Eggelpoël, M.J., Chettouh, H., Fartoux, L., Aoudjehane, L., Barbu, V., Rey, C., Priam, S., Housset, C., Rosmorduc, O., and Desbois-Mouthon, C. (2012). Epidermal growth factor receptor and HER-3 restrict cell response to sorafenib in hepatocellular carcinoma cells. J. Hepatol. *57*, 108–115. https://doi.org/10.1016/j.jhep.2012.02.019.

51. Love, M.I., Huber, W., and Anders, S. (2014). Moderated estimation of fold change and dispersion for RNA-seq data with DESeq2. Genome Biol. *15*, 550. https://doi.org/10.1186/s13059-014-0550-8.

52. Bayard, Q., Meunier, L., Peneau, C., Renault, V., Shinde, J., Nault, J.C., Mami, I., Couchy, G., Amaddeo, G., Tubacher, E., et al. (2018). Cyclin A2/E1 activation defines a hepatocellular carcinoma subclass with a rearrangement signature of replication stress. Nat. Commun. *9*, 5235. https://doi.org/10.1038/s41467-018-07552-9.

53. Hirsch, T.Z., Negulescu, A., Gupta, B., Caruso, S., Noblet, B., Couchy, G., Bayard, Q., Meunier, L., Morcrette, G., Scoazec, J.Y., et al. (2020). BAP1 mutations define a homogeneous subgroup of hepatocellular carcinoma with fibrolamellar-like features and activated PKA. J. Hepatol. *72*, 924–936. https://doi.org/10.1016/j.jhep.2019.12.006.

54. Rebouissou, C., Sallis, S., and Forné, T. (2022). Quantitative Chromosome Conformation Capture (3C-qPCR). Methods Mol. Biol. *2532*, 3–13. https://doi.org/10.1007/978-1-0716-2497-5_1.

55. Ea, V., Sexton, T., Gostan, T., Herviou, L., Baudement, M.O., Zhang, Y., Berlivet, S., Le Lay-Taha, M.N., Cathala, G., Lesne, A., et al. (2015). Distinct polymer physics principles govern chromatin dynamics in mouse and Drosophila topological domains. BMC Genomics *16*, 607. https://doi.org/10.1186/s12864-015-1786-8.

56. Corces, M.R., Buenrostro, J.D., Wu, B., Greenside, P.G., Chan, S.M., Koenig, J.L., Snyder, M.P., Pritchard, J.K., Kundaje, A., Greenleaf, W.J., et al. (2016). Lineage-specific and single-cell chromatin accessibility charts human hematopoiesis and leukemia evolution. Nat. Genet. *48*, 1193–1203. https://doi.org/10.1038/ng.3646.

57. Buenrostro, J.D., Wu, B., Chang, H.Y., and Greenleaf, W.J. (2015). ATAC-seq: A Method for Assaying Chromatin Accessibility Genome-Wide. Curr. Protoc. Mol. Biol. *109*, 21–29. https://doi.org/10.1002/0471142727.mb2129s109.

58. Corces, M.R., Trevino, A.E., Hamilton, E.G., Greenside, P.G., Sinnott-Armstrong, N.A., Vesuna, S., Satpathy, A.T., Rubin, A.J., Montine, K.S., Wu, B., et al. (2017). An improved ATAC-seq protocol reduces background and enables interrogation of frozen tissues. Nat. Methods *14*, 959–962. https://doi.org/10.1038/nmeth.4396.

59. Tran, S., Baba, I., Poupel, L., Dussaud, S., Moreau, M., Gélineau, A., Marcelin, G., Magréau-Davy, E., Ouhachi, M., Lesnik, P., et al. (2020). Impaired Kupffer Cell Self-Renewal Alters the Liver Response to Lipid Overload during Non-alcoholic Steatohepatitis. Immunity *53*, 627–640.e5. https://doi.org/10.1016/j.immuni.2020.06.003.

YMTHE, Volume *32*

Supplemental Information

DLK1/*DIO3* locus upregulation by a β-catenin-dependent enhancer drives cell proliferation and liver tumorigenesis

Julie Sanceau, Lucie Poupel, Camille Joubel, Isabelle Lagoutte, Stefano Caruso, Sandra Pinto, Christèle Desbois-Mouthon, Cécile Godard, Akila Hamimi, Enzo Montmory, Cécile Dulary, Sophie Chantalat, Amélie Roehrig, Kevin Muret, Benjamin Saint-Pierre, Jean-François Deleuze, Sophie Mouillet-Richard, Thierry Forné, Christophe F. Grosset, Jessica Zucman-Rossi, Sabine Colnot, and Angélique Gougelet

Supplemental material

Table S1: Top 20 overexpressed RNAs in Apc$^{\Delta hep}$ *versus* wild-type or βcatenin$^{\Delta hep}$ hepatocytes from RNAseq data. Results are represented as the log2 fold induction in Apc$^{\Delta hep}$ *versus* wt hepatocytes (second column) and versus β-catenin$^{\Delta hep}$ **(**βcat$^{\Delta hep}$) hepatocytes (fourth column) with their respective pvalue (pval). RNAs produced from the *Dlk1/Dio3* locus are indicated in bold and grey.

gene	Log2 Apc$^{\Delta hep}$ / wt	pval	Log2 Apc$^{\Delta hep}$/βcat$^{\Delta hep}$	pval
Eln	10.6	5.9E-42	20.0	1.0E-50
Wisp2	9.3	1.0E-50	10.8	1.0E-50
Akr1c18	7.8	4.0E-16	7.7	2.8E-23
Rian	**7.6**	**1.0E-50**	**20.0**	**1.0E-50**
Nkd1	7.5	1.0E-50	7.4	1.0E-50
AK133155	7.3	1.1E-27	7.8	1.0E-43
Slpi	7.1	1.0E-50	7.2	1.0E-50
Rtl1	**6.8**	**7.1E-10**	**20.0**	**4.4E-15**
Akr1b7	6.6	1.0E-50	8.4	1.0E-50
Meg3	**6.5**	**1.0E-50**	**13.5**	**1.0E-50**
Pkp1	6.5	7.0E-13	20.0	7.4E-21
Prom1	6.5	2.1E-13	5.9	2.1E-18
Prr18	6.4	7.3E-13	20.0	9.6E-21
Kif26b	6.2	5.3E-38	9.7	1.0E-50
Trib2	6.1	4.0E-31	6.7	1.0E-50
BC023483	6.1	4.3E-02	5.0	4.2E-02
Mirg	**6.1**	**4.5E-26**	**20.0**	**1.0E-50**
Reep1	6.1	1.7E-14	6.7	4.6E-22
Ihh	6.1	6.5E-30	9.2	1.0E-50
Elovl7	5.9	3.2E-06	20.0	1.5E-09

Table S2: Top 20 overexpressed miRNAs in Apc$^{\Delta hep}$ *versus* wt hepatocytes from small-RNAseq data. Results are represented as the log2 fold induction in Apc$^{\Delta hep}$ *versus* wt hepatocytes (second column) or versus βcat$^{\Delta hep}$ (fourth column) with their respective adjusted pvalue (padj). MiRNAs produced from the *Dlk1/Dio3* locus are indicated in bold and grey.

miRNA	Log2 Apc$^{\Delta hep}$ / wt	padj	Log2 Apc$^{\Delta hep}$/bcat$^{\Delta hep}$	padj
mmu-miR-341	**6.7**	**4.3E-31**	**7.0**	**1.8E-60**
mmu-miR-665	**6.7**	**4.5E-26**	**8.7**	**1.9E-53**
mmu-miR-136	**6.7**	**1.8E-69**	**8.2**	**2.2E-140**
mmu-miR-433	**6.4**	**1.7E-17**	**7.5**	**1.5E-29**
mmu-miR-377	**5.9**	**6.5E-07**	**10.0**	**2.0E-09**
mmu-miR-329	**5.9**	**2.7E-07**	**5.0**	**7.6E-08**
mmu-miR-127	**5.9**	**2.9E-51**	**7.7**	**6.3E-130**
mmu-miR-431	**5.8**	**3.6E-22**	**7.4**	**2.0E-47**
mmu-miR-370	**5.7**	**4.4E-18**	**7.4**	**1.5E-35**
mmu-miR-487b	**5.4**	**8.2E-11**	**5.5**	**1.7E-15**
mmu-miR-434-3p	**5.4**	**4.3E-31**	**7.7**	**4.3E-92**
mmu-miR-496	**5.4**	**6.1E-08**	**6.4**	**6.3E-11**
mmu-miR-381	**5.4**	**1.1E-26**	**6.5**	**6.5E-65**
mmu-miR-434-5p	**5.3**	**1.3E-29**	**7.7**	**4.9E-90**
mmu-miR-543	**5.2**	**6.7E-13**	**10.0**	**1.1E-25**
mmu-miR-376a	**5.2**	**1.3E-17**	**5.9**	**1.3E-35**
mmu-miR-376b	**5.2**	**2.9E-21**	**6.5**	**1.7E-50**
mmu-miR-134	**5.2**	**3.4E-32**	**6.0**	**5.1E-77**
mmu-miR-495	**5.1**	**1.2E-11**	**5.1**	**1.0E-17**
mmu-miR-409-3p	**5.0**	**1.4E-26**	**6.4**	**1.3E-71**

Table S3: pathological and molecular characteristics of the pediatric cohort 1

Patient	Samples	Gender	Age (months)	TV	VI	S/MN	M	SC	CH	P	CHIC-HS	Risk	AFP (ng/mL)	ß-catenin RNAseq
P02	T/NT	F	11	60	N	S	N	N	Y	II	B	SR	153840	exon3 del
P04_a	T/NT	F	14	197	N	S	N	N	N	II	B	SR	300	exon3 del
P04_c	T/NT	F	14	197	N	S	N	N	Y	II	B	SR	300	exon3 del
P09	T	F	6	160	N	S	N	N	Y	III	B	NA	401807	exon3 del
P15	T/NT	M	5	760	N	S	N	N	Y	II	B	SR	56613	exon3 del
P16	T/NT	M	36	800; 500	Y	M	N	N	Y	IV	D	HR	54982	WT
P17	T/NT	M	12	520	N	S	N	Y	Y	II	B	SR	837000	exon3 del
P19	T/NT	M	9	2	N	S	N	Y	Y	I	B	HR	88000	in frame deletion aa15-
P20	T/NT	F	12	41	N	S	N	N	Y	II	B	SR	318800	D32V
P22	NT	F	NA	2	Y	M	Y	Y	Y	III	D	HR	2000000	G34V
P23	T/NT	M	50	4	Y	M	Y	Y	Y	II	D	HR	350000	in frame deletion aa25-
P24	T/NT	M	4	5	N	M	N	Y	Y	III	C	SR	82000	S37A
P26_b	T/NT	M	28	2 805	Y	M	Y	Y	Y	II	D	HR	1500000	in frame deletion aa37-
P27	T/NT	F	NA	598	N	S	N	N	Y	II	B	SR	2355000	G34V
P28	T/NT	F	11	1 540	Y	M	N	Y	Y	IV	C	HR	360000	exon3 del
P29	T/NT	F	NA	NA	N	S	N	N	N	II	A	NA	300	in frame deletion aa19-
P32	T/NT	F	4	1	N	S	N	N	Y	II	B	SR	934371	WT
P33	T/NT	M	10	241	N	M	N	Y	Y	III	C	SR	300000-500000	in frame deletion aa28-
P34	T	M	4	520	N	S	N	N	Y	III	B	SR	518000	T41A
P35	T/NT	F	24	912	Y	M	N	Y	Y	II	C	HR	1000000	G34E
P36	T/NT	M	130	NA	N	S	N	N	Y	IV	D	HR	NA	WT
P38	T/NT	M	11	1 584	N	S	N	N	Y	II	B	NA	155385	exon3 del

CH: chemotherapy
HR: high risk
NA: non available
M: metastasis
P: PRETEXT stage
SC: Small Cells presence
S/MN: solitary/multiple nodules
SR: standard risk
TV: Tumor volume (cm^3)
VI: vascular invasion
Children's Hepatic Tumors International Collaboration-Hepatoblastoma Stratification

Table S4: Clinical, pathological and molecular characteristics of the pediatric cohort 2 (n=110) from previously published series [1]

Variable		Total (%)
Age (months)	[median. min-max]	33 (3-278)
Gender	Male : Female	65 (59%) : 45 (41%)
Sample Type	Primary hepatoblastoma	83 (75%)
	Hepatoblastoma relapse	3 (3%)
	Hepatoblastoma metastasis	14 (13%)
	Hepatocellular carcinoma	10 (9%)
Etiology	Without known etiology	94 (85%)
	Other*	16 (15%)
Chemotherapy	yes	84 (76%)
	no	26 (24%)
Transcriptomic group	Hepatocyte 1	21 (25%)
	Hepatocyte 2	19 (23%)
	Liver Progenitor	33 (40%)
	Mesenchymal	10 (12%)
***CTNNB1* mutations**	Mutated	92 (92%)
	Non-mutated	8 (8%)

*Beckwith Wiedmann Syndrome; Familial Adenomatous Polyposis; Mitochondrial Cytopathy. Progressive familial intrahepatic cholestasis. Tyrosinemia. Simpson Golabi Behmel Syndrome.

Table S5: Top 20 under-expressed RNAs in Apc$^{\Delta hep}$-DLK1/DIO3$^{\Delta WRE}$ *versus* Apc$^{\Delta hep}$-Rosa26 hepatocytes from RNAseq data. Results are represented as the log2 fold induction in Apc$^{\Delta hep}$-DLK1/DIO3$^{\Delta WRE}$ *versus* Apc$^{\Delta hep}$-Rosa26 hepatocytes and their respective adjusted p-value (padj). RNAs produced from the *Dlk1/Dio3* locus are indicated in bold and grey.

gene	Log2 Apc$^{\Delta hep}$ DLK1/DIO3$^{\Delta WRE}$/ Apc$^{\Delta hep}$ Rosa26	p-adj
Oxtr	-5.12	2.0E-03
Gm37899	**-2.81**	**9.0E-03**
Gm27000	-2.81	2.0E-03
B830012L14Rik	**-2.65**	**1.0E-02**
Hba-a1	-2.63	4.0E-02
Drp2	-2.61	1.0E-02
Mirg	**-2.49**	**3.5E-08**
Rtl1	**-2.47**	**4.5E-07**
Rian	**-2.29**	**2.4E-16**
Gm12248	-2.05	2.0E-02
Meg3	**-2.03**	**6.0E-03**
Depdc1a	-1.9	4.0E-03
Col6a3	-1.75	5.0E-03
Gm48302	-1.75	3.0E-02
Cenpf	-1.7	3.0E-02
Cip2a	-1.69	3.0E-05
Melk	-1.69	8.0E-03
Nuf2	-1.61	2.0E-03
Kif20b	-1.61	3.0E-03
Pla2r1	-1.58	2.0E-04

Table S6: Top 20 under-expressed miRNAs in Apc$^{\Delta hep}$-DLK1/DIO3$^{\Delta WRE}$ *versus* Apc$^{\Delta hep}$-Rosa26 hepatocytes from small RNAseq data. Results are represented as the log2 fold induction in Apc$^{\Delta hep}$-DLK1/DIO3$^{\Delta WRE}$ *versus* Apc$^{\Delta hep}$-Rosa26 hepatocytes and their respective adjusted p-value (padj). miRNAs produced from the *Dlk1/Dio3* locus are indicated in bold.

miRNA	Log2 Apc$^{\Delta hep}$ DLK1/DIO3$^{\Delta WRE}$ / Apc$^{\Delta hep}$ Rosa26	p-adj
mmu-miR-337-5p	**0.47**	**2.3E-05**
mmu-miR-127-3p	**0.47**	**2.9E-05**
mmu-miR-154-5p	**0.47**	**1.4E-04**
mmu-miR-299a-3p	**0.48**	**8.4E-04**
mmu-miR-543-3p	**0.48**	**1.1E-03**
mmu-miR-134-5p	**0.51**	**9.1E-05**
mmu-miR-496a-3p	**0.52**	**6.1E-03**
mmu-miR-154-3p	**0.52**	**8.6E-03**
mmu-miR-409-3p	**0.53**	**2.6E-04**
mmu-miR-434-5p	**0.54**	**2.7E-03**
mmu-miR-379-3p	**0.54**	**4.5E-03**
mmu-miR-376b-3p	**0.54**	**6.2E-03**
mmu-miR-434-3p	**0.56**	**5.8E-04**
mmu-miR-1193-3p	**0.56**	**5.0E-03**
mmu-miR-494-3p	**0.57**	**3.7E-03**
mmu-miR-299b-3p	**0.57**	**1.4E-02**
mmu-miR-376a-3p	**0.57**	**1.7E-02**
mmu-miR-136-5p	**0.57**	**2.5E-02**
mmu-miR-337-3p	**0.57**	**3.5E-02**
mmu-miR-376a-5p	**0.57**	**3.6E-02**

Table S7: Most significantly under-expressed RNAs in Apc$^{\Delta hep}$-DLK1/DIO3$^{\Delta WRE}$ *versus* Apc$^{\Delta hep}$-Rosa26 hepatocytes from RNAseq data. Results are represented as the log2 fold induction in Apc$^{\Delta hep}$-DLK1/DIO3$^{\Delta WRE}$ *versus* Apc$^{\Delta hep}$-Rosa26 hepatocytes and their respective adjusted p-value (padj). RNAs produced from the *Dlk1/Dio3* locus are indicated in bold and grey and those involved in cell cycle process in red.

gene	Log2 Apc$^{\Delta hep}$ DLK1/DIO3$^{\Delta WRE}$ / Apc$^{\Delta hep}$ Rosa26	p-adj
Rian	**-2.29**	**2.4E-16**
Mirg	**-2.49**	**3.5E-08**
Rtl1	**-2.47**	**4.5E-07**
Kif20a	-1.36	3.0E-06
Cip2a	-1.69	3.0E-05
Pla2r1	-1.58	2.0E-04
Ifi213	-1.12	2.0E-03
Gm27000	-2.81	2.0E-03
Nuf2	-1.61	2.0E-03
Ccnb1	-1.22	2.0E-03
Ckap2	-1.52	2.0E-03
Oxtr	-5.12	2.0E-03
Top2a	-0.99	2.0E-03
Thrsp	-1.03	2.0E-03
Kif4	-0.99	2.0E-03
Nedd4l	0.62	3.0E-03
Kif20b	-1.61	3.0E-03
Ccna2	-1.04	3.0E-03
Depdc1a	-1.9	4.0E-03
Hmmr	-1.27	4.0E-03
Nusap1	-1.22	4.0E-03
Slc25a30	1.42	5.0E-03
Rbpms	0.89	5.0E-03
Mndal	-0.97	5.0E-03
Col6a3	-1.75	5.0E-03
Meg3	**-2.03**	**6.0E-03**
Melk	-1.69	8.0E-03
Gm37899	**-2.81**	**9.0E-03**
Racgap1	-0.95	1.0E-02
Drp2	-2.61	1.0E-02
Pdilt	-0.70	1.0E-02
Atp8a1	-1.08	1.0E-02
Mir99ahg	-1.55	1.0E-02
B830012L14Rik	**-2.65**	**1.0E-02**
Slc34a2	-1.12	2.0E-02
Gm12248	-2.05	2.0E-02
Foxa2	0.82	2.0E-02
Rnf144a	1.27	2.0E-02
Cdca3	-0.82	2.0E-02
Mgat4b	0.72	2.0E-02
Flot1	0.60	2.0E-02
Chic1	-0.80	2.0E-02
Slc33a1	-0.48	2.0E-02
Gm48302	-1.75	3.0E-02
Insig1	-0.75	3.0E-02

Foxa3	0.45	3.0E-02
Cenpf	-1.7	3.0E-02
Zxda	1.24	3.0E-02
mt-Atp6	-0.75	3.0E-02
Cdk1	-0.76	4.0E-02
Hba-a1	-2.63	4.0E-02
Gas2l3	-0.98	4.0E-02
Rasa2	1.16	4.0E-02
Gm32540	2.45	4.0E-02
Hmga1b	4.97	4.0E-02
Rab35	0.57	4.0E-02
Ncapg2	-1.23	5.0E-02

Table S8: RNAseq data for regulators of cell cycle progression and cytokinesis. Results are represented as the log2 fold induction in $Apc^{\Delta hep}$ *versus* wild-type hepatocytes and $Apc^{\Delta hep}$-DLK1/$DIO3^{\Delta WRE}$ *versus* $Apc^{\Delta hep}$-Rosa26 hepatocytes and their respective adjusted p-value (padj); in green: down-regulation. in orange: up-regulation.

gene	Log2 $Apc^{\Delta hep}$ vs wt	pvalue	Log 2 $Apc^{\Delta hep}$ DLK1/$DIO3^{\Delta WRE}$ vs $Apc^{\Delta hep}$	padj
Kif4	2.7	1E-05	-1.0	2E-03
Kif20a	2.4	1E-10	-1.4	3E-06
Kif20b	3.9	1E-06	-1.6	2E-03
Nuf2	3.1	4E-05	-1.6	3E-03
Nusap1	2.8	4E-05	-1.2	4E-03
Top2a	2.8	3E-12	-1.0	2E-03
Gas2l3	1.4	1E-02	-1.0	4E-02
Cenpf	2.9	8E-10	-1.7	3E-02
Ckap2	3.1	3E-08	-1.5	2E-03
Depdc1a	2.2	1E-02	-1.9	4E-03
Hmmr	2.1	2E-05	-1.3	4E-03
Racgap1	2.8	1E-07	-1.0	1E-02
Pla2r1	3.1	2E-03	-1.6	2E-04
Rasa2	1.3	6E-02	1.1	4E-02
Flot1	1.0	2E-03	0.6	2E-02
Ccna2	2.3	6E-07	-1.2	2E-03
Ccnb1	2.3	4E-03	-1.2	2E-03
Cdk1	2.6	1E-07	-0.7	4E-02

Table S9: lists of primers and probes used

Name	Sequence	Supplier
Ctnnb1-I2-3	5'-TCAGTATGAGCTCCATGGGAC AGGGGT-3'	Eurogentec[1]
Ctnnb1-I3-1	5'-GACAGCTCAGCCACAGCACAA GTGGGT-3'	Eurogentec[1]
Rosa-1	5'-CTCGATGGAAAATACTCCGAG GCGGAT-3'	Eurogentec[1]
sg2 DLK1-WRE (mouse)	5'- TTCCTCAGTGGGGCTAAAGGA GAGGGT -3'	Eurogentec[1]
Sg5 DLK1-WRE (mouse)	5'- GGATGACCTTTGACTTCTGAA GGGAGT -3'	Eurogentec[1]
Sg1 DLK1-WRE (human)	5'- TATTCAGAGCAAGCCTGTGGC ATGAAT -3'	Eurogentec[1]
Sg2 DLK1-WRE (human)	5'- TACCCTTTAGGTGTTTGCGGA AAGGAT -3'	Eurogentec[1]
Sg3 DLK1-WRE (human)	5'- GCAGGACCCTTCTCAAAGGGC CAGGGT -3'	Eurogentec[1]
Sg3 DLK1-WRE (human)	5'- CTTTGCAGTCGTGAACTGTGG GGGGAT -3'	Eurogentec[1]
Rosa26 editing	F 5'-CTTGCTCTCCCAAAGTCGCT-3' R 5'-CCAATGCTCTGTCTAGGGGT-3'	Eurogentec[1]
Ctnnb1 editing	F 5'-TTTTGGTGTCGGGGCACATA-3' R 5'-CATGGTGCGTACAATGGCAG-3'	Eurogentec[1]
DLK1-WRE editing (mouse)	F 5'-AGCATGGCCGAGTACTCATT-3' R 5'-CCTCTGCATGACCTGTGACT-3'	Eurogentec[1]
DLK1-WRE editing (human)	F 5'-TGAGGCTGCAATGAACCATG-3' R 5'-GGCTTATGTTGTGCAAACGC-3'	Eurogentec[1]
18S	F 5'-GTAACCCGTTGAACCCCATT-3' R 5'-CCATCCAATCGGTAGTAGCG -3'	Eurogentec[1]
Mirg	F 5'-A GCCATCTACCTCTGAGTCCC-3' R 5'-AGAGCAGAAACCCCTCCTTC-3'	Eurogentec[1]
Rian	F 5'-CCAGGTTCAAGGTCCCTCAT-3' R 5'-TCTTGTGTCTCGAAGGCCTT-3'	Eurogentec[1]
Mki67	F 5'-CTGCCTGCGAAGAGAGCATC-3' R 5'-AGCTCCACTTCGCCTTTTGG-3'	Eurogentec[1]
Kif20a	F 5'-AAGTGGTGAGCGGCTAAAGGAG-3' R 5'-GAAGCCTTGGAACACACGAGTC-3'	Eurogentec[1]
Kif20b	F 5'-GGATGACCTAGACGTGCTTACC-3' R 5'-TCGCTTGAGTGGTAAGGACAGC-3'	Eurogentec[1]
Nuf2	F 5'-CCTCTATGGTCAGAATGCAGCAG-3' R 5'-ACTGCTTGAACTCCTCTCGCTC-3'	Eurogentec[1]
Nusap1	F 5'-TTCCTCCAAGAGGAAGGCTCTC-3' R 5'-GGTGTCTTGGTCAGTGAGCACT-3'	Eurogentec[1]
Top2a	F 5'-CAAGCGAGAAGTGAAGGTTGCC-3' R 5'-GCTACCCACAAAATTCTGCGCC-3'	Eurogentec[1]
Cenpf	F 5'- GCACGACTTCAGTTACAGGAGC -3' R 5'- TGCTTTGGTGTTTTCTCTGTAGTC -3'	Eurogentec[1]
Ckap2	F 5'- TACTGACCAGCGCAGATACACG -3' R 5'- TCCTTTGCCAGTTCTCCACTCC-3'	Eurogentec[1]
Ccna2	F 5'- GCCTTCACCATTCATGTGGAT -3' R 5'- TTGCTCCGGGTAAAGAGACAG-3'	Eurogentec[1]
Fadd	F 5'-CACACAATGTCAAATGCCACCTG-3' R 5'-TGCGCCGACACGATCTACTGC-3'	Eurogentec[1]
Ccl2	F 5'-TCTGGGCCTGCTGTTCACA-3' R 5'-GGATCATCTTGCTGGTGAATGA-3'	Eurogentec[1]
Ccl5	F 5'-GCTGCTTTGCCTACCTCTCC-3' R 5'-TCGAGTGACAAACACGACTGC-3'	Eurogentec[1]
Csf1	F 5'-TACAAGTGGAAGTGGAGGAGCCAT-3' R 5'-AGTCCTGTGTGCCCAGCATAGAAT- 3'	Eurogentec[1]
Human FADD	F 5'-ATTAATGCCTCTCCCGCACC-3' R 5'-TCTCTGCTTCGCTCCGATTC-3'	Eurogentec[1]
DLK1-WRE (ChIP)	F 5'-CCTCTTCCTGCCCCTAACGTA-3' R 5'-CCTGTGTCTGGATGACCTTTGA -3'	Eurogentec[1]
Myc-10kb (ChIP control)	F 5'- ACACACCTTGAATCCCGT -3'	Eurogentec[1]

	R 5'- CCCAGCTAGAATGAACAAG -3'	
Kif20a (ChIP)	F 5'- GGT-AAC-CCG-GAC-CCA-CAT-TA -3' R 5'- TGA-TCC-CAG-CTT-CTA-CCC-AC -3'	Eurogentec[1]
Ccna2 (ChIP)	F 5'- CTT-TCT-CTG-TGA-TGC-TGC-CA -3' R 5'- GGG-GTG-GGG-TAG-TTT-ACT-GG -3'	Eurogentec[1]
Cdc2 (ChIP)	F 5'- CGA-GTG-CCA-GCA-GTT-TCA-AA -3' R 5'- GAG-CTC-AAG-AGT-CAG-TTG-GC -3'	Eurogentec[1]
Cenpf (ChIP)	F 5'- ACGAGCGATTCAAACTGCC -3' R 5'- CCAAAAGGGCCAATCAGAGG -3'	Eurogentec[1]
Ig-DMR (ChIP)	F 5'-GACACCCTGCCTTCTCTCTT-3' R 5'-TTCCCTACTGCCCTTCCTTG-3'	Eurogentec[1]
human CCNA2 (ChIP)	F 5'-AGTTCAAGTATCCCGCGACT-3' R 5'-CCCAGCCAGTTTGTTTCTCC-3'	Eurogentec[1]
human KIF20A (ChIP)	F 5'-GGTAACCCGGACCCACATTA-3' R 5'-TTACTCACACCTAGTCGCCG-3'	Eurogentec[1]
human CDC2 (ChIP)	F 5'-TGCTCCGCTGACTAGAAAC-3' R 5'-GTTTCAAACTCACCGCGCTA-3'	Eurogentec[1]
F1 (3C)	F 5'- TCCCTCCAAGGTAAGAGCCCG -3' R 5'- AGGGACAAACTTGGCAGCAGTC -3'	Eurogentec[1]
F14 (3C)	F 5'- CTGCATGGGCAGACAAGGACC -3' R 5'- CAGGCAGCCACTACTACAGAAG -3'	Eurogentec[1]
F33 (3C)	F 5'- GCTCAACGAAGAGATCAGGCAC -3' R 5'- GCATCCATCCAGGCTACGCTTC -3'	Eurogentec[1]
F16 (DLK1-WRE. 3C)	5'- CTCCCTCCACGGCTCAGATC-3'	Eurogentec[1]
F4 (3C)	5'-GGCAGGTATAGCATCATACTCCC-3'	Eurogentec[1]
F5 (3C)	5'-CATGTCCCATGTGGCCACTTGC-3'	Eurogentec[1]
F10 (3C)	5'-CTATCTCCAAGTGGTCTTGGCC-3'	Eurogentec[1]
F11 (3C)	5'-GATGAGCGTGGCACTCAGACC-3'	Eurogentec[1]
F12 (3C)	5'-CCACATCTGGCCAGTGCTTGC-3'	Eurogentec[1]
F17 (3C)	5'-CTTGGTTCACCCATCCTTGGCC-3'	Eurogentec[1]
F20 (3C)	5'-GCAGTAGTAGCACCTGCTGGTC-3'	Eurogentec[1]
F21 (3C)	5'-GCTCAGAGCTGGAGAGACAGAC-3'	Eurogentec[1]
F22 (3C)	5'-CCATGCTATTGGAGGTCCTGGG-3'	Eurogentec[1]
F23 (3C)	5'-CCTGGGTGCCCCCAAAATACAC-3'	Eurogentec[1]
F24 (3C)	5'-GTGGGCCATTTCTGCAGGGTG-3'	Eurogentec[1]
F31 (3C)	5'-CAGCACTCGGTTCTGCTACCAG-3'	Eurogentec[1]
F32 (3C)	5'-GACCAAGGGTTTCATGGGGCAG-3'	Eurogentec[1]
F34 (3C)	5'-CTGCTGCAAGGTTTGGAGGATG-3'	Eurogentec[1]
Meg3 (in situ hybridization)	Sens: 5'AAGAAGACTGAGGACCCCAGGA-3' Antisens 5'-TGTGTCCGTGTGTCCAGGGT-3'	Eurogentec[1]
miR-127 probe (in situ hybridization)	MIMAT0004604	Exiqon/ Thermo Fisher[2]
Hsa-miR-127	000452	Thermo Fisher[2]
sno135	001230	Thermo Fisher[2]
Meg3 mouse	Mm00522599	Thermo Fisher[2]
MEG3 human	Hs00292028	Thermo Fisher[2]
Glul mouse	Mm00725701	Thermo Fisher[2]
GLUL human	Hs00365928_g1	Thermo Fisher[2]
Apc total form	Mm00545877	Thermo Fisher[2]
Apc deleted form	Mm01130462	Thermo Fisher[2]
human RIAN (MEG8)	Hs00419701_m1	Thermo Fisher[2]
human MIRG (MEG9)	Hs01593046_s1	Thermo Fisher[2]
mouse Rian	Mm01325842_g1	Thermo Fisher[2]
mouse Mirg	Mm01335848	Thermo Fisher[2]
human RTL-1	Hs06637009_s1	Thermo Fisher[2]
mouse Rtl-1	Mm02392620_s1	Thermo Fisher[2]
DLK1-WRE (ChIP)	ART2AUJ	Thermo Fisher[2]
Afp-220kb (ChIP control)	AJHSN1G	Thermo Fisher[2]

[1] Eurogentec, Seraing, Belgium, [2]Thermofischer, Waltham, MA

Table S10: lists of antibodies and kits used

WB: western-blot. IHC: Immunohistochemistry

Name	Supplier	Reference	Quantity/Dilution
Glutamine synthétase	BD Biosciences, Franklin Lakes, NJ	610518	1/400 (IHC)
Ki67	Abcam, Cambridge, UK	Ab16667	1/300 (IHC)
Cleaved Caspase 3	Cell Signaling, Danvers, MA	#9661	1/600 (IHC)
DLK1	Proteintech, San Diego, CA	10636-1-AP	1/1000 (WB)
Cyclin A2	Abcam, Cambridge, UK	ab 32386	1/100 (WB)
Cyclin B1	Cell Signaling, Danvers, MA	4138	1/200 (WB)
FOXM1	Santa Cruz Biotechnology, Dallas, TX	sc-376471 X	10ug (CHIP) , 1/100 (IHC)
CD45 -PE	BD Biosciences, Franklin Lakes, NJ	553081	1/400 (flow cytometry)
CD31 – BV605	BioLegend, San Diego, CA	102427	1/300 (flow cytometry)
CD11b – BV510	BD Biosciences, Franklin Lakes, NJ	562950	1/400 (flow cytometry)
CD11c – PE Cy.7	BD Biosciences, Franklin Lakes, NJ	558079	1/400 (flow cytometry)
F4/80 – Percp Cy 5.5	Thermofischer, Waltham, MA	130-118-466	1/300 (flow cytometry)
Ly6C – V450	BD Biosciences, Franklin Lakes, NJ	560594	1/200 (flow cytometry)
Ly6G – APC Cy.7	BioLegend, San Diego, CA	127624	1/200 (flow cytometry)
TCF-4	Millipore, Burlington, MA	05-511	3ug (CHIP)
β-catenin	BD Biosciences Franklin Lakes, NJ	610154	1/50 (IHC), 10µg (CHIP)
HNF-4α	Santa-Cruz, Dallas, TX	sc-6556x	10µg (CHIP)
H3K27ac	Active Motif, Carlsbad, CA	39133	10µg (CHIP)
H3K4me3	Active Motif, Carlsbad, CA	39159	5 µg (CHIP)
H3K4me1	Active Motif, Carlsbad, CA	39297	10µg (CHIP)
β-actin	Sigma-Aldrich, Saint-Louis, CA	A5441	1/5000 (WB)
FADD	Elabscience, Houston, TX	E-AB-10318	1/1000 (WB)
mouse on mouse kit	Vector Lab, Newark, CA	BMK2202	
Anti-rabbit biotinylated	Vector Lab, Newark, CA	BA-1000	1/200 (IHC)
Histofine kit	Microm Microtech, Brignais, France	F/414341F	
Anti-rabbit HRP	Cell Signaling, Danvers, MA	7074	1/2000 (WB)
Anti-mouse HRP	Cell Signaling, Danvers, MA	7076	1/2000 (WB)

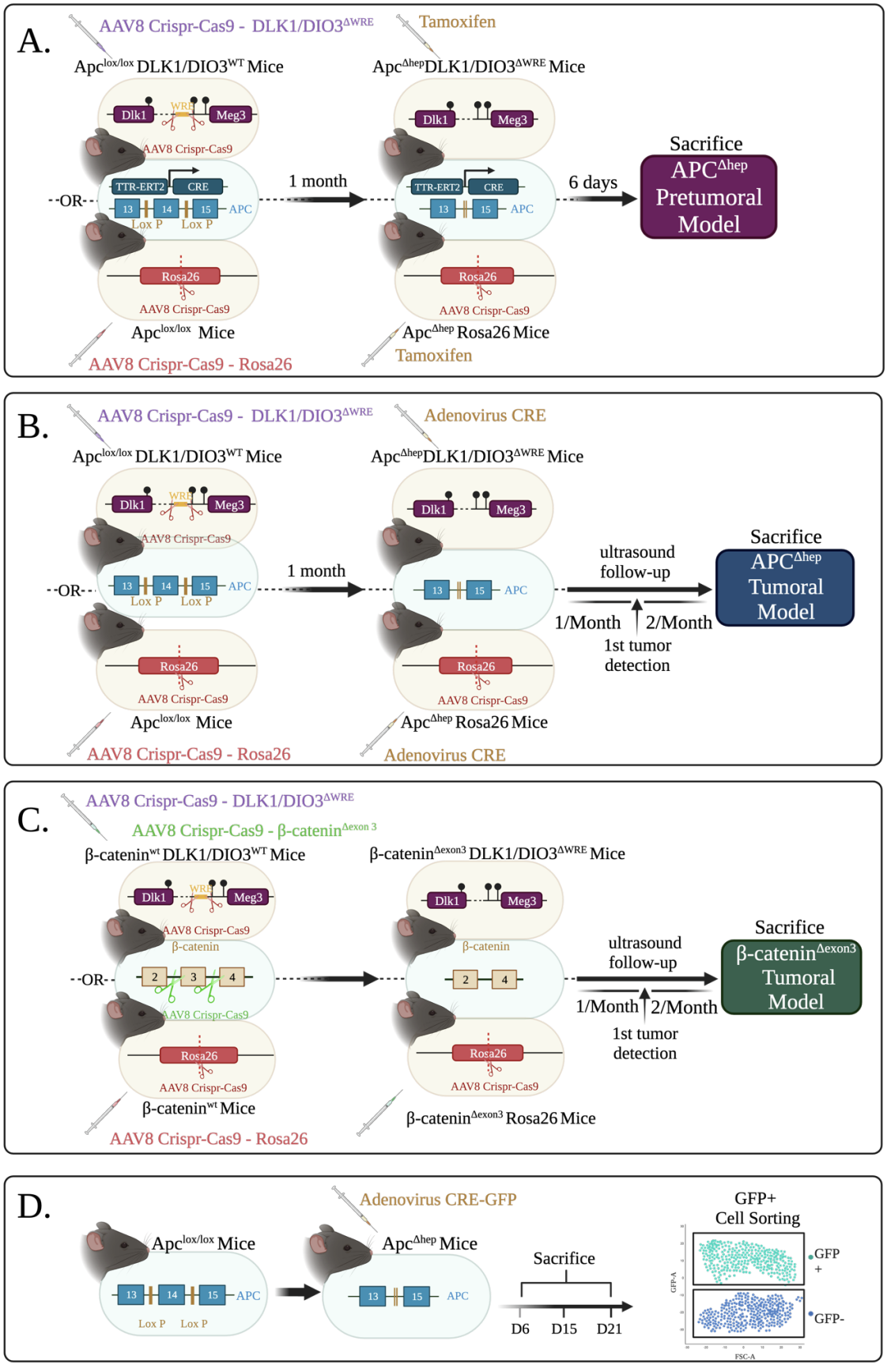

Figure S1: Schematic representation of experimental models

A-B: Generation of $Apc^{\Delta hep}$-DLK1/$DIO3^{\Delta WRE}$ model with AAV8 CRISPR/Cas9 constructs targeting the DLK1-WRE site in $Apc^{lox/lox}$ model: tamoxifen-induced *Apc* deletion was conducted one month after AAV8 injection, which is the time that we have identified as optimal for gene editing[2] in pretumoral model (**A**) and tumoral model (**B**); **C:** Generation of β-$catenin^{\Delta Exon3}$ DLK1/$DIO3^{\Delta WRE}$ model with concomitant injection of AAV8 CRISPR/Cas9 constructs targeting *Ctnnb1* and the DLK1-WRE site; **D:** Kinetics of hepatocyte sorting: GFP-positive hepatocytes were sorted from tumoral $Apc^{\Delta hep}$ livers in early-steps by flow cytometry (ARIA3, BD). GFP- and GFP+ hepatocytes from $Apc^{wt/wt}$ mice were used as control hepatocytes. Figure made with Biorender.

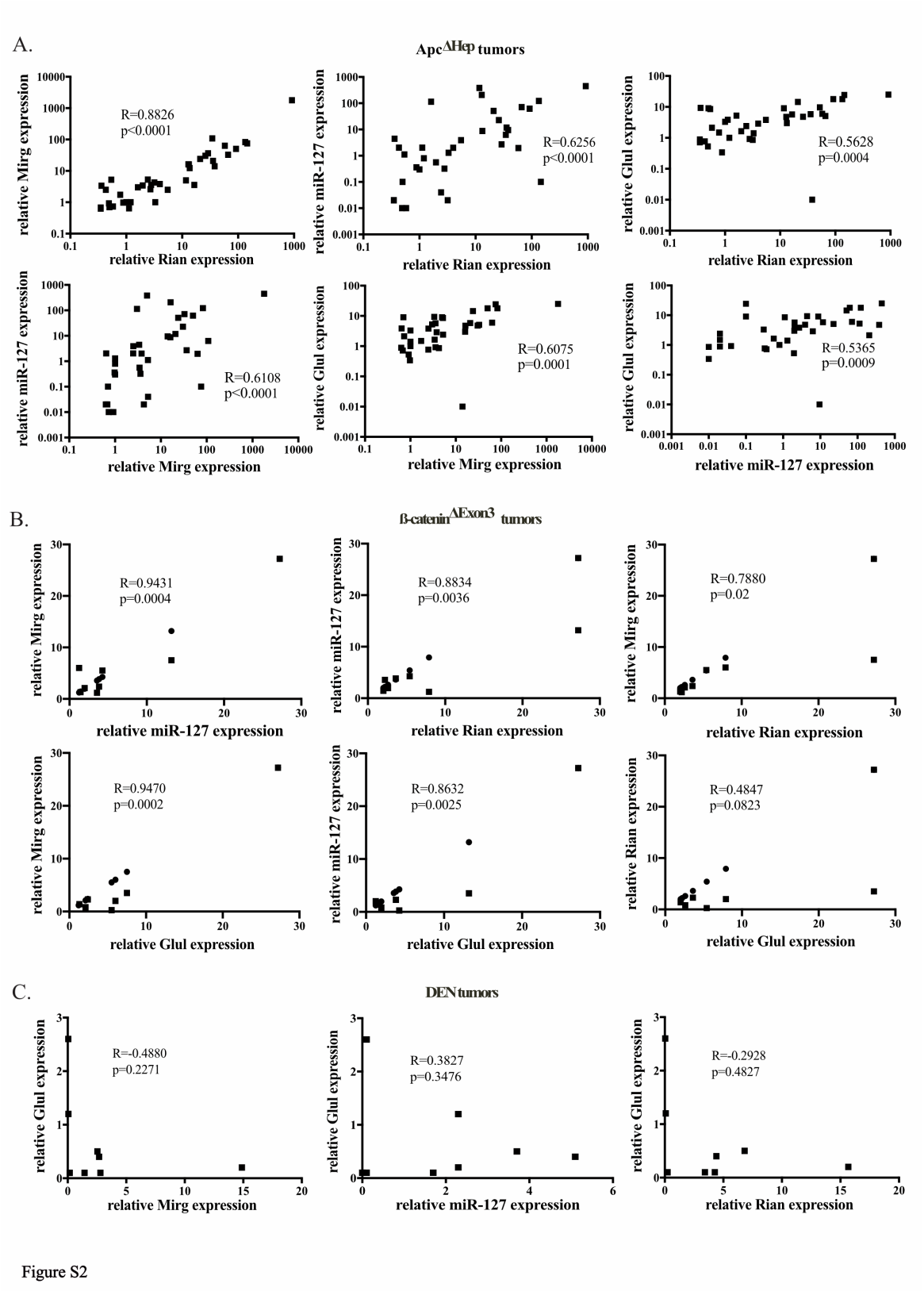

Figure S2

Figure S2: Correlation between expression levels of RNAs within the *Dlk1/Dio3* locus and *Glul* in Apc$^{\Delta hep}$, β-catenin$^{\Delta Exon3}$ and DEN tumors

A-C: Correlation between *Rian*, *Mirg,* miR-127, and *Glul* expression levels by RT-qPCR in Apc$^{\Delta hep}$ tumors (**A),** β-catenin$^{\Delta Exon3}$ tumors (**B**), and DEN tumors (**C**).

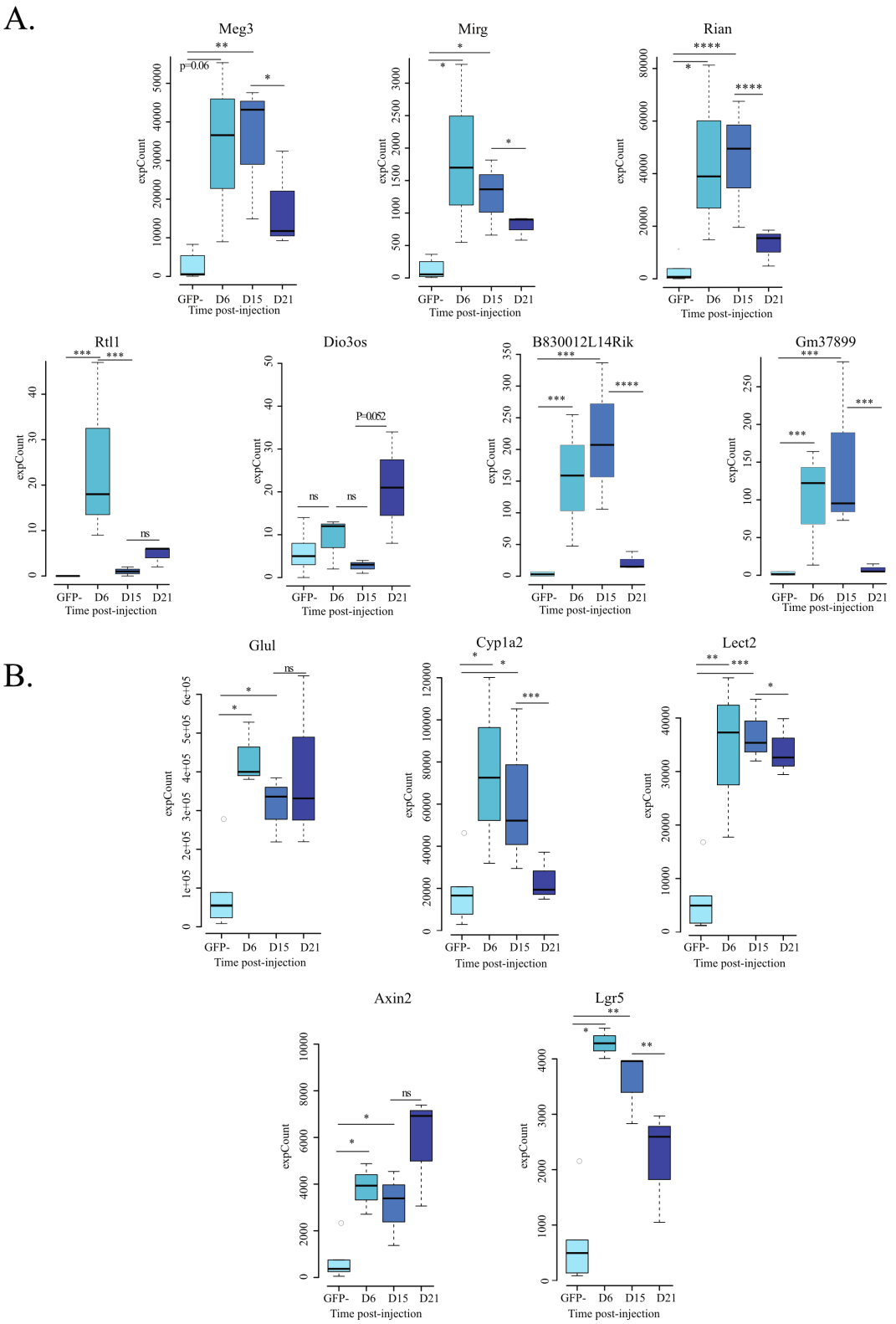

Figure S3

Figure S3: RNAs within the *Dlk1/Dio3* locus are induced during the earliest phases of tumorigenesis in Apc$^{\Delta hep}$ model

A-B: RNA-seq data analyses from sorted hepatocytes at day 6, 15 and day 21 after injection of an adenovirus Cre-GFP and subsequent activation of β-catenin signaling in $Apc^{\Delta hep}$ model. Box plots represent the mean normalized RPKM of at least three independent samples; **A:** RNAs from the *DLK1/DIO3* locus; **B:** canonical target genes of β-catenin. Levels of significance: *p<0.05, ** p<0.01, ***p<0.005, ****p<0.0001, ns: non-significant (Mann-Whitney), with error bars representing s.e.m..

.

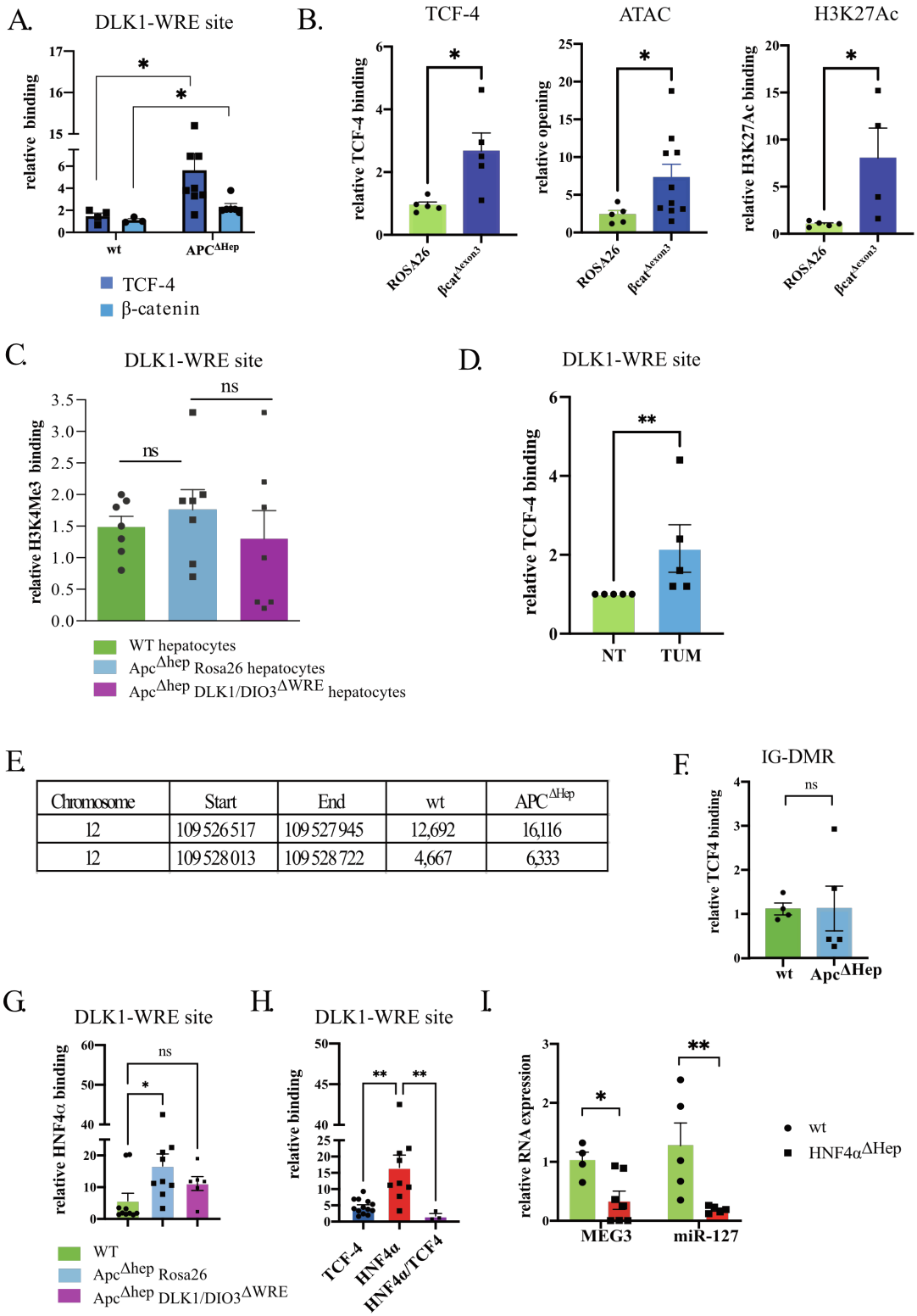

Chromosome	Start	End	wt	APC$^{\Delta Hep}$
12	109526517	109527945	12,692	16,116
12	109528013	109528722	4,667	6,333

Figure S4

Figure S4: ChIP- and ATAC-qPCR validations

A: ChIP-qPCR analysis of β-catenin and TCF-4 binding at the DLK1-WRE site in wild-type (wt) and $Apc^{\Delta hep}$ hepatocytes relative to isotype control; **B:** ChIP-qPCR analysis of TCF-4 and H3K27ac relative binding to isotype control and ATAC-qPCR performed in Rosa26 (green) and β-$catenin^{\Delta Exon3}$ hepatocytes (blue); **C:** ChIP-qPCR analysis of H3K4me3 marks at DLK1-WRE site in wt, $Apc^{\Delta hep}$-Rosa26 and $Apc^{\Delta hep}$-DLK1/$DIO3^{\Delta WRE}$ hepatocytes binding to isotype control; **D:** ChIP-qPCR analysis of TCF-4 binding at the DLK1-WRE site in $Apc^{\Delta hep}$ and β-$catenin^{\Delta Exon3}$ tumors (TUM) compared to isotype control and adjacent non-tumor tissues (NT); **E:** methylation status of IG-DMR obtained by MeDIP-seq (GSE239777) in $Apc^{\Delta hep}$ *versus* wild-type hepatocytes; **F:** ChIP-qPCR analysis of TCF-4 binding at the IG-DMR site in $Apc^{\Delta hep}$ *versus* wt hepatocytes relative to isotype control; **G**: HNF4α binding at the DLK1-WRE site in wt, $Apc^{\Delta hep}$-Rosa26 and $Apc^{\Delta hep}$-DLK1/$DIO3^{\Delta WRE}$ hepatocytes relative to isotype control; **H:** sequential ChIP-qPCR analysis for HNF4α and TCF-4 at the DLK1-WRE site in $Apc^{\Delta hep}$-Rosa26 hepatocytes relative to isotype control; **I:** *Meg3* and miR-127 expression determined by RT-qPCR in $HNF4\alpha^{\Delta hep}$ hepatocytes. Levels of significance: *$p<0.05$, ** $p<0.01$, ns: non-significant (Mann-Whitney or Kruskal-Wallis), with error bars representing s.e.m..

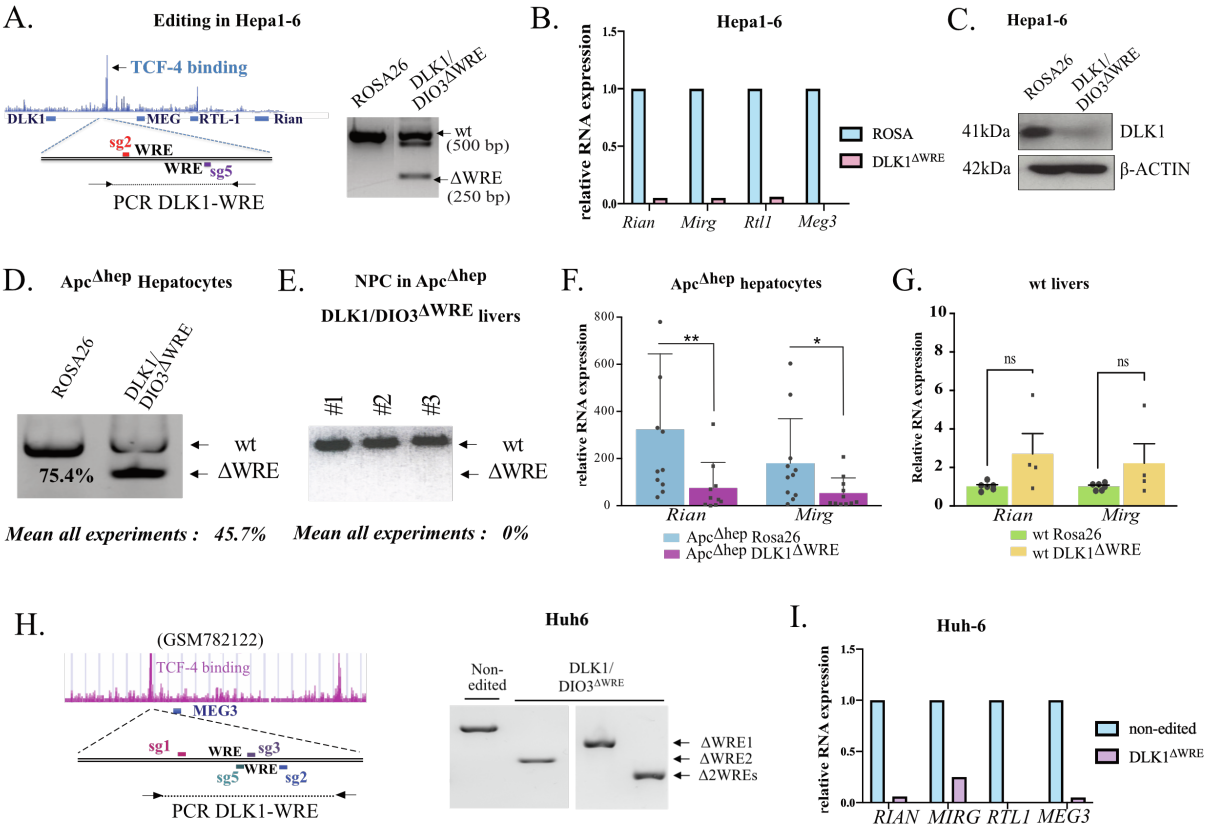

Figure S5

Figure S5: Validation of CRISPR/Cas9 constructs in hepatic cancer cell lines and in Apc$^{\Delta hep}$ livers *in vivo*

A: Design of 2 sgRNAs to delete the TCF-4 binding site upstream of *Meg3* (left panel) and representative PCR analysis of the DLK1-WRE region showing the deleted band (ΔWRE) and the full band (WT) (right panel) in Hepa1-6 clones; **B:** *Rian, Mirg, Meg3,* and *Rtl1* expression determined by RT-qPCR in DLK1/DIO3$^{\Delta WRE}$ Hepa1-6 clones compared to Rosa26 controls; **C:** DLK1 protein level determined by Western-blot in Hepa1-6 clones; **D:** Efficiency of CRISPR/Cas9 editing by AAV8 injection *in vivo* on isolated Apc$^{\Delta hep}$-Rosa26 and Apc$^{\Delta hep}$-DLK1/DIO3$^{\Delta WRE}$ hepatocytes. A representative PCR analysis of the DLK1-WRE region is shown with quantification of the deleted band with ImageJ as well as the mean of all experiments indicated below **E:** representative PCR analysis of the DLK1-WRE region showing no deleted band on three samples of non-parenchymal cells (NPCs) isolated from Apc$^{\Delta hep}$-DLK1/DIO3$^{\Delta WRE}$ livers; **F-G:** Relative expression of *Rian* and *Mirg* by RT-qPCR in isolated Apc$^{\Delta hep}$-DLK1/DIO3$^{\Delta WRE}$ *versus* Apc$^{\Delta hep}$-Rosa26 hepatocytes compared to wild-type hepatocytes (**F**) and in wt-DLK1/DIO3$^{\Delta WRE}$ livers compared to wt-Rosa26 livers (**G**); **H**:

Design of 4 sgRNAs to delete the TCF-4 binding site upstream of *MEG3*, which contains 2 WREs identified from the publicly available ChIP-seq data targeting TCF-4 in the human hepatoblastoma HepG2 cell line (Gsm782122) (left panel); representative PCR analysis showing the deleted band (ΔWRE) in DLK1/DIO3$^{\Delta WRE}$ Huh6 clones for three couples of sgRNAs deleting one or both WREs (right panel); the two PCR images show all types of clones emerging in a 96-well plate and thus originate from distinct regions of the same gel of screening; **I:** *MEG3*, *MIRG*, *RTL-1,* and *RIAN* expression by RT-qPCR in DLK1/DIO3$^{\Delta WRE}$ Huh6 clones compared to non-edited Huh6 control clones. Levels of significance: *$p<0.05$, ** $p<0.01$, ns: non-significant (Mann-Whitney), with error bars representing s.e.m..

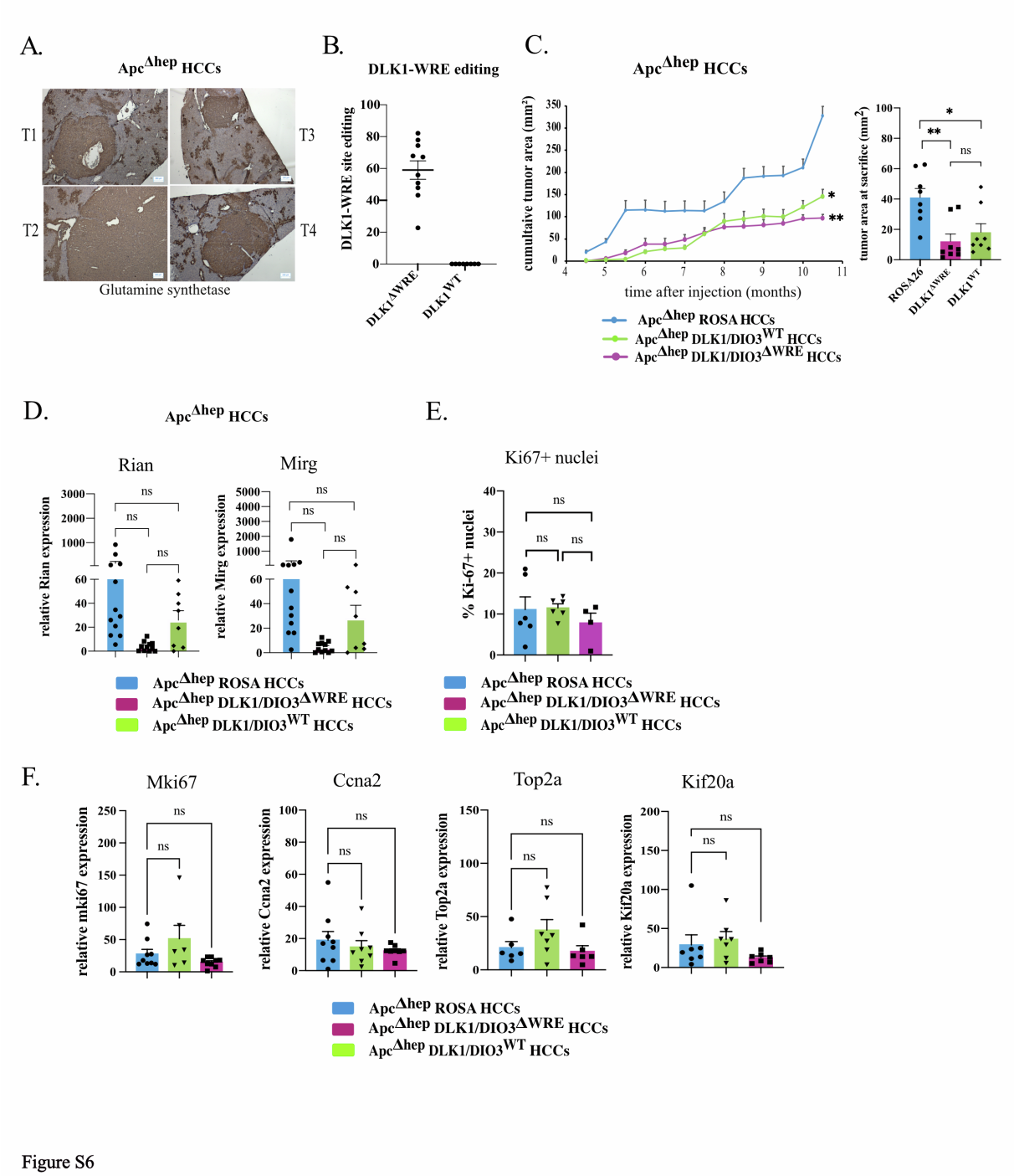

Figure S6

Figure S6: DLK1-WRE site editing slows Apc$^{\Delta hep}$ HCC growth but does not affect the expression of the identified actors involved in G2/M phase

A: Examples of glutamine synthetase staining of Apc$^{\Delta hep}$ HCCs; **B:** analysis of tumor editing by PCR band quantification with ImageJ in Apc$^{\Delta hep}$ HCC; **C:** Progression of cumulative tumor areas (left panel) and areas at sacrifice (right panel) for Apc$^{\Delta hep}$ HCC; **D:** RT-qPCR analysis of *Rian* and *Mirg* expression in Apc$^{\Delta hep}$ HCC compared to their adjacent non-tumor tissues; **E**: Percentage of Ki-67+ hepatocytes in Apc$^{\Delta hep}$ HCC; **F:** Expression of *Mki67*, *Ccna2*, *Top2a*, and

Kif20a determined by RT-qPCR relative to their adjacent non-tumor tissues in $Apc^{\Delta hep}$ HCC. Levels of significance: *p<0.05, ** p<0.01, ns: non-significant (Kruskal-Wallis), with error bars representing s.e.m..

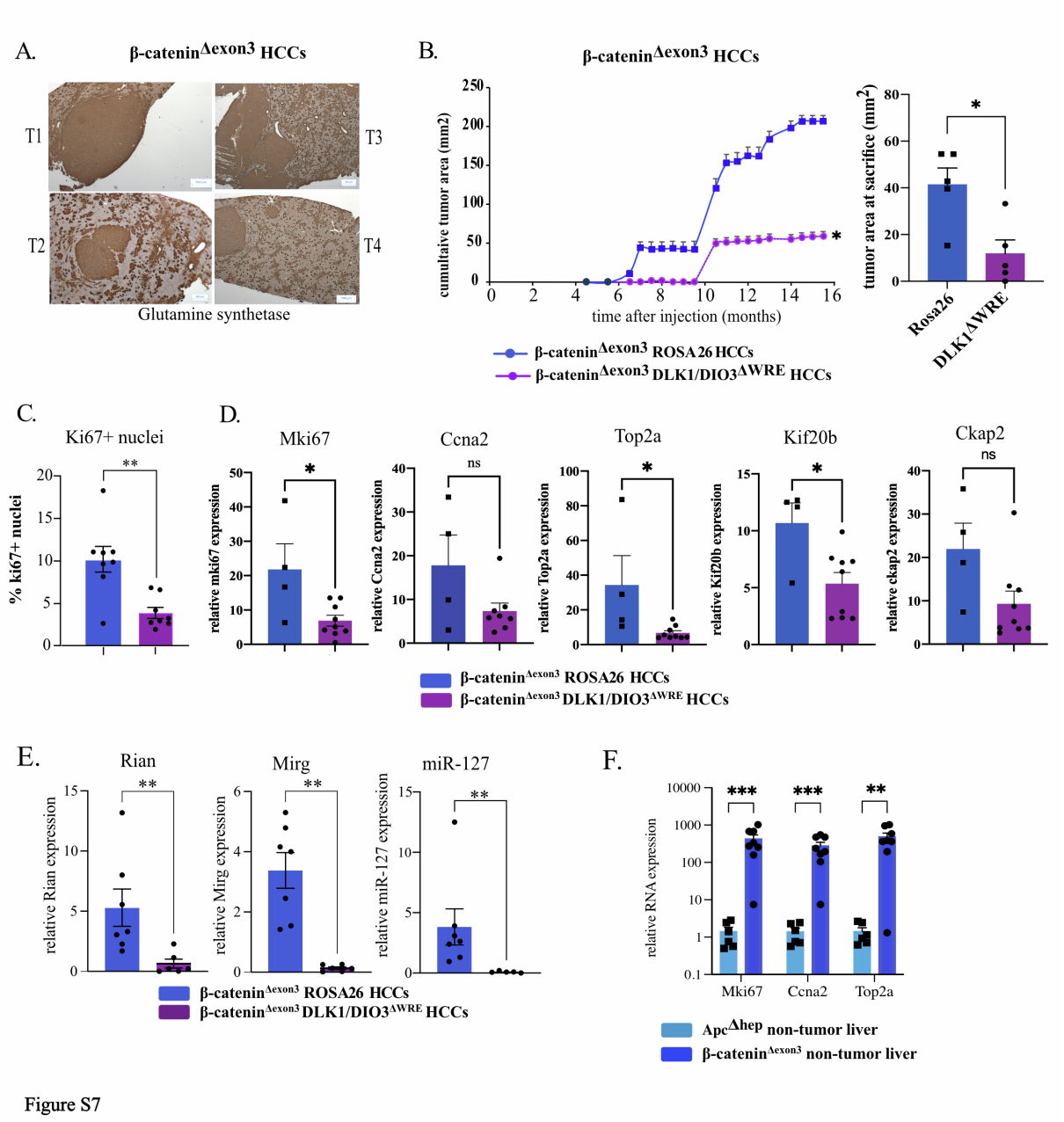

Figure S7

Figure S7: DLK1-WRE site editing slows β-catenin$^{\Delta Exon3}$ HCC growth

A: Examples of glutamine synthetase staining of β-catenin$^{\Delta Exon3}$ HCC; **B**: Progression of cumulative tumor areas (left panel) and areas at sacrifice (right panel) for β-catenin$^{\Delta Exon3}$ HCC; **C:** Percentage of Ki-67+ hepatocytes in β-catenin$^{\Delta Exon3}$ HCC; **D:** Expression of *Mki67*, *Ccna2*, *Top2a*, *Kif20b,* and *Ckap2* determined by RT-qPCR in β-catenin$^{\Delta Exon3}$ HCC relative to their adjacent non-tumor tissues; **E:** RT-qPCR analysis of *Rian*, *Mirg* and miR-127 in β-catenin$^{\Delta Exon3}$ HCC compared to their adjacent non-tumor tissues; **F:** RT-qPCR analysis of *Mki67*, *Ccna2* and *Top2a* in Apc$^{\Delta hep}$ and β-catenin$^{\Delta Exon3}$ non-tumor tissues. Levels of significance: *p<0.05,

**p<0.01, *** p<0.005, ns: non-significant (Mann-Whitney), with error bars representing s.e.m..

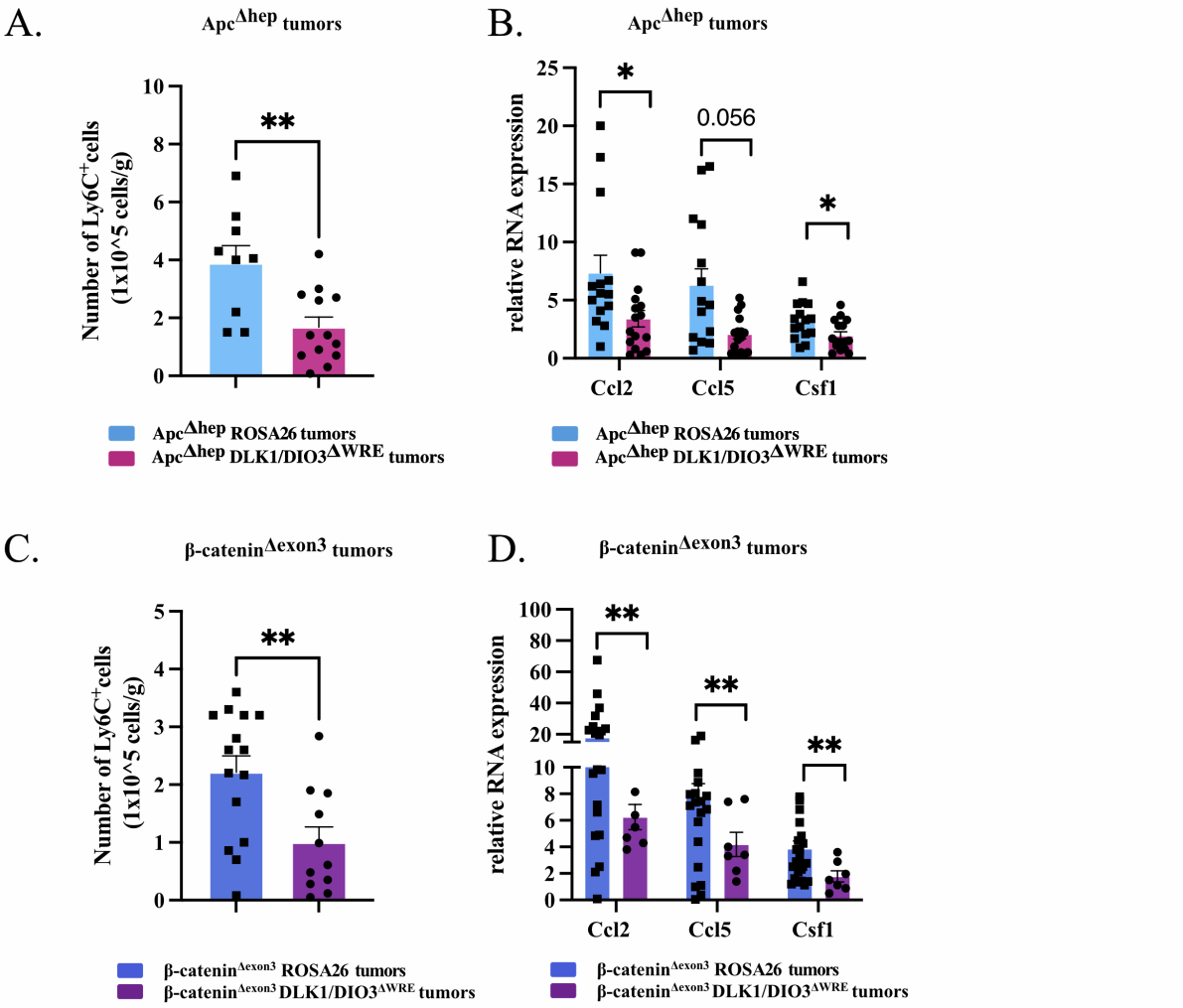

Figure S8

Figure S8: DLK1-WRE site editing impairs monocyte recruitment in Apc$^{\Delta hep}$ and β-catenin$^{\Delta Exon3}$ tumors.

A, C: Absolute number of Ly6C+ monocytes relative to tissue weight in Apc$^{\Delta hep}$ (**A**) and β-catenin$^{\Delta Exon3}$ tumors (**C**); **B, D:** RT-qPCR analysis of *Ccl2*, *Ccl5*, and *Csf1* relative to their adjacent non-tumor tissues in Apc$^{\Delta hep}$ tumors (**B**) and β-catenin$^{\Delta Exon3}$ tumors (**D**). Levels of significance: *p<0.05, ** p<0.01 (Mann-Whitney), with error bars representing s.e.m..

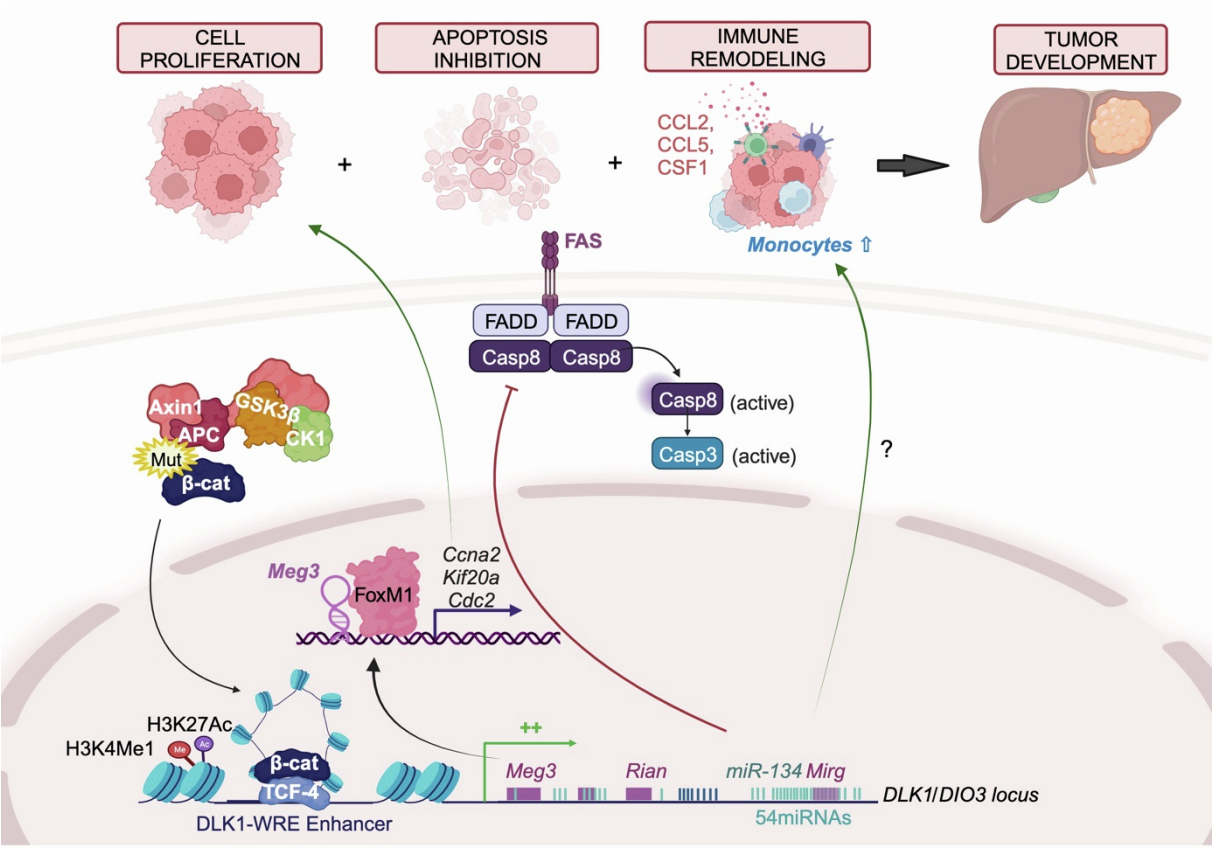

Figure S9: Graphical abstract

Figure made with Biorender.

References:

1. Hirsch, T. Z., Pilet, J., Morcrette, G., Roehrig, A., Monteiro, B. J. E., Molina, L., Bayard, Q., Trepo, E., Meunier, L., Caruso, S. *et al.* Integrated Genomic Analysis Identifies Driver Genes and Cisplatin-Resistant Progenitor Phenotype in Pediatric Liver Cancer. (2021). Cancer Discov. 11, 2524-2543, doi:10.1158/2159-8290.CD-20-1809
2. Loesch, R., Caruso, S., Paradis, V., Godard, C., Gougelet, A., Renault, G., Picard, S., Tanaka, I., Renoux-Martin, Y., Perret, C. *et al.* Deleting the beta-catenin degradation domain in mouse hepatocytes drives hepatocellular carcinoma or hepatoblastoma-like tumor growth. (2022). J Hepatol. doi:10.1016/j.jhep.2022.02.023